A MULTI-PROXY STALAGMITE RECORD OF PALEOENVIRONMENTAL CHANGE IN EQUATORIAL AFRICA DURING THE AFRICAN HUMID PERIOD

by

LAURA A. DUPONT

(Under the Direction of L. Bruce Railsback)

ABSTRACT

A multi-proxy record from U-Th dated Stalagmite MAT-12 from Matupi Cave (1.19°N, 30.01°E) in northeastern Democratic Republic of Congo provides a reconstruction of the paleoenvironmental effects of the African Humid Period (AHP) in central equatorial Africa. Results from stable isotope analysis ($\delta^{13}C$, $\delta^{18}O$) and petrographic analysis (mineralogy, layer specific width, and layer-bounding surfaces) are paired with a high-resolution radiometric U-Th age model to reveal the local response to the AHP, a climate event of the late Pleistocene to mid-Holocene, 14,800 to 5500 yr BP. Though the 1300-year record from Stalagmite MAT-12 is somewhat brief and only covers a portion of the AHP, it provides a detailed reconstruction of changes in vegetation and rainfall near Matupi Cave while Stalagmite MAT-12 was deposited. This reconstruction makes notable contributions to the current understanding of the geographic extent, timing, and causes of the AHP in central equatorial Africa.

INDEX WORDS: Paleoenvironment, Paleoclimate, African Humid Period, Stalagmite, Equatorial Africa, Democratic Republic of Congo, Multiple proxy, Stable isotopes, Petrography

A MULTI-PROXY STALAGMITE RECORD OF PALEOENVIRONMENTAL CHANGE IN EQUATORIAL AFRICA DURING THE AFRICAN HUMID PERIOD

by

LAURA A. DUPONT

B.S., University of Georgia, 2017

B.A., University of Georgia, 2017

A Thesis Submitted to the Graduate Faculty of The University of Georgia in Partial Fulfillment of the Requirements for the Degree

MASTER OF SCIENCE

ATHENS, GEORGIA

2021

A MULTI-PROXY STALAGMITE RECORD OF PALEOENVIRONMENTAL CHANGE IN EQUATORIAL AFRICA DURING THE AFRICAN HUMID PERIOD

by

LAURA A. DUPONT

Major Professor:	L. Bruce Railsback
Committee:	Douglas E. Crowe
	David F. Porinchu
	George A. Brook

Electronic Version Approved:

Ron Walcott
Vice Provost for Graduate Education and Dean of the Graduate School
The University of Georgia
May 2021

ACKNOWLEDGEMENTS

My success in the completion of this thesis would not have been possible without the exemplary mentorship of my advisor, Dr. Bruce Railsback. His extensive scientific knowledge was instrumental in producing this thesis as he devoted countless hours to guiding me through both my graduate and undergraduate research projects. From presentations to publications, his mentorship allowed me to accomplish goals I thought were outside of my abilities. I would also like to acknowledge the efforts of my committee members, Dr. Doug Crowe, Dr. Dave Porinchu, and Dr. George Brook for their assistance and valuable suggestions. My gratitude extends to all of the professors of the University of Georgia Geology Department, whose lectures, laboratories, and field trips made my experience worthwhile. The three classes I took with Dr. Steve Holland stand out most as his pedagogy is unmatched. I am glad to call Dr. Sally Walker a friend as she has supported my work since I entered the Geology Department in 2015. I thank one professor in Marine Sciences, Dr. Christof Meile, who has also been a great friend and supporter in the final year of my studies.

To my mentors and friends at the Center for Applied Isotope Studies: I am so grateful for the time I have spent with you all. I thank my supervisor, Emmy Deng, for her patience and flexibility as I completed my degrees. I am grateful for the time she invested in instructing me in laboratory procedures that were outside my discipline. My work as a graduate student would not have been possible without the support and mentorship of Tom

Maddox, who promoted my skills as a laboratory scientist and allowed me to realize my enthusiasm for water quality science.

I also thank my parents, Jon and Julie Dupont, and my sister, Ashley Dupont, for their encouragement and unwavering support. My sister's decision to become a geologist led me down a similar path for my undergraduate degrees, and I am grateful that she has paved the way for me more than once in my life. The financial contributions of my extended family, most notably my grandparents Patricia and Frank Repp, made my travel to present my research at the Summer for Speleothem Science Conference in Burgos, Spain possible. My attendance at this conference solidified my decision to pursue graduate studies and boosted my confidence in my scientific abilities, and so made all the difference. The support from my family down south, Bennett, Judy, and Mrs. Constance Threlkeld was also an invaluable comfort when things got tough. To my partner, Cullen Threlkeld, thank you for supporting me as you were also tasked with completing a graduate degree. Our double-trouble duo Pico and Cilantro made 2020 bearable.

My gratitude knows no depth. Thank you all.

TABLE OF CONTENTS

Page

LIST OF TABLES

Page

LIST OF FIGURES

Page

CHAPTER 1: INTRODUCTION

Over the past 40 years, paleoenvironmental reconstructions have increasingly applied data collected from stalagmites (Fairchild and Baker, 2012). Widespread use of stalagmite data became a reliable and useful option through the development of precise U-Th dating on small sample masses via mass spectrometry (Edwards et al., 1987). While many reconstructions center on the application of stable isotope data, the unique petrography of stalagmite layers presents an opportunity for a multi-proxy approach. Most recently, stalagmite studies have made a significant contribution as climate archives by precisely dating and delineating shifts in hydroclimate and vegetation. Stalagmite $\delta^{18}O$ values have been most popularly employed to track the hydroclimate response on the global, regional, and local level to climate change events (McDermott, 2004; Lachniet, 2009; Wong and Breecker, 2015), but stalagmite $\delta^{13}C$, growth rate, layer-specific width, and layer-bounding surfaces can also be utilized to reconstruct past climate.

This study expands the sampling of an already-collected specimen, Stalagmite MAT-12, from Matupi Cave in northeastern Democratic Republic of Congo (DRC). Here, a multi-proxy approach is used to reconstruct the paleoenvironmental conditions in central equatorial Africa during the African Humid Period (AHP), a climate event of increased wetness in Africa from ca. 5.5 to 14.8 kyr BP. The objective of this study was to answer two questions: 1) How did rainfall amount and vegetation cover change near Matupi Cave during the AHP, and 2) How does this new record of the AHP at Matupi Cave compare to other paleoenvironmental records in equatorial Africa?

The text herein attempts to be as specific as possible when defining the differences between AHP sites in Africa, while duly recognizing that inherent differences in the proxies utilized may also lead to different climate signals. The contributions of the future co-authors of the Stalagmite MAT-12 manuscript, Dr. L. Bruce Railsback, Dr. George A. Brook, Dr. Fuyuan Liang, Dr. Ny Riavo Voarintsoa, Dr. Hai Cheng, and Dr. R. Lawrence Edwards, are recognized most specifically in the methods chapter.

1.1. Stalagmites and paleoclimate reconstruction

Stalagmites are speleothems, or secondary cave deposits, that form when $CaCO_3$ precipitates on the floor of a cave from dripwater (Fig. 1). The fundamental equation for stalagmite formation is:

$$Ca^{2+}_{(aq)} + 2HCO_3^-{}_{(aq)} \leftrightarrow CaCO_{3\,(s)} + CO_{2\,(g)} + H_2O_{(l)}$$

The formation and erosion of stalagmites depends largely upon water availability, where water is the main dissolution and transport agent. An increase in Ca^{2+} drives this equation to the right towards precipitation, and an increase in CO_2 of the cave air and/or H_2O within the cave drives this equation to the left towards dissolution.

The precipitation of $CaCO_3$ primarily occurs by the degassing of CO_2 as the dripwater enters the cave. CO_2 degassing occurs when high-PCO_2 water from the epikarst encounters low-PCO_2 air within the cave. Degassing causes the pH of the dripwater to increase, which subsequently increases the concentration of CO_3^{2-} to precipitate $CaCO_3$. Less commonly, $CaCO_3$ precipitation is driven by the evaporation of dripwater as it enters the cave. Evaporation increases the Ca^{2+} and/or the CO_3^{2-} concentration of the dripwater. Evaporation within the cave requires a low relative humidity, and because most caves are

often very humid, $CaCO_3$ precipitation by evaporation is far less likely than $CaCO_3$ precipitation by degassing.

All components of stalagmite formation are controlled by the conditions of the water supply that passes through the epikarst and into the cave as dripwater. In particular, the residence time of the dripwater is relevant in that if the water passes through the epikarst too quickly to dissolve the carbonate bedrock and/or enters the cave too quickly to degas, it will not be saturated with respect to $CaCO_3$ and so cannot precipitate $CaCO_3$. This case of increased water supply, as well as a case of decreased water supply, are controlled by changes in rainfall, runoff, and evaporation in the stalagmite's catchment. Seasonality also comes into play in summer-rainfall zones as more water enters the system during warmer, rainy seasons and less water enters the system during colder, drier seasons. Thus, changes in the climatology of the region and the hydrogeology of the epikarst system can impede or promote stalagmite growth. The result of both non-deposition due to drier conditions and erosion due to wetter conditions causes some amount of time to be unaccounted for in the stalagmite's layers and becomes a hiatus in time-series reconstructions. Both scenarios may be recorded as layer-bounding surfaces in the $CaCO_3$ layers that indicate dissolutional erosion or lessened deposition prior to those hiatuses (Railsback et al., 2013). Vegetation also plays a role in stalagmite formation as it provides the soil CO_2 via root respiration—a key element to the formation of the carbonic acid that dissolves the limestone to form the Ca^{2+} and HCO_3^- that are carried by the dripwater. This suggests that vegetation type and cover influence the formation of a stalagmite. Vegetation type and cover are primarily controlled by the regional climate of the overlying cave system, but human activity can also alter the environment in a significant way that can control and be recorded by

stalagmites (e.g., Voarintsoa et al., 2017; Railsback et al., 2020). In sum, the water supply of the hydrological system of the epikarst and the condition of vegetation overlying the cave, which are both strongly influenced by changes in regional climate, exert control on the formation of stalagmites.

Unfortunately, stalagmite formation is also controlled, at least in part by, changes in the cave resulting from collapses of the cave's roof and at the cave's opening. Paleoclimatologists nonetheless hope that changes in stalagmite characteristics reflect changes in regional climate and are therefore useful paleoenvironmental proxies. It follows that proxy interpretations should be carefully applied depending on the environmental characteristics of the overlying region and that selection of stalagmites for paleoenvironmental reconstruction should consider the quality and the position of that stalagmite within the cave system.

1.2. The African Humid Period

The African Humid Period (AHP) is a well-documented climate event of the late Pleistocene to mid-Holocene ca. 5.5 to 14.8 kyr BP (deMenocal et al., 2000). During the AHP, much of northern and eastern Africa was wetter than today, and the environment within and near the modern Sahara Desert accommodated several large and small lakes where savannah plant and animal species were prevalent (e.g., McIntosh and McIntosh, 1983; Willis et al. 2013). Though various proxy records have demonstrated the orbitally-forced, pluvial nature of the AHP, the spatial and temporal patterns of AHP onset, intensity, and termination have been subject to intense debate (Costa et al., 2014). Here, a thorough,

but certainly not exhaustive, explanation of the current understanding of the geographic extent, the timing of, and the causes of the AHP is outlined.

1.2.1. Geographic extent of the African Humid Period

The spatial patterns of the AHP cannot be clearly defined without agreement of the terms used to describe the regions in question. In this study, the African continent was divided into four regions that have similar hydroclimate: northern Africa, western Africa, southern Africa, and equatorial Africa (Fig. 2). Equatorial Africa is split into two subregions due to the diversity of modern environmental conditions: central equatorial Africa and eastern equatorial Africa, where eastern Africa is further split into northeastern equatorial and southeastern equatorial Africa (Fig. 2). Explicit definitions of these regions and their distinctions in terms of AHP conditions is prudent to ensure clarity.

Here, the terms northern, western, and southern Africa arise out of the distinction that these places are not similar to equatorial Africa, the region focused on in this study. The term **northern Africa** is used to describe all sites above 15°N (Fig. 2). Many, if not all, of these sites remain dry year-round. These were the first sites that identified the AHP, and many focused on the pluvial conditions reconstructed from paleolake data and near-shore marine cores (e.g., deMenocal et al., 2000; Gasse et al., 2002; Lézine et al., 2011; Zielhofer et al., 2017). These publications report data collected from various sites as far as 33°N in the mid-Atlas of Morocco, as far west as 18°W off the coast of Mauritania, and as far as 32°E in eastern Sudan.

Sites in **western Africa** lie south of 15°N, west of 15°E, and north of 15°S (Fig. 2). Many sites in the region are wettest in June–August and driest in December–February.

While the AHP can be identified in western Africa, the results from those studies and those in northern Africa are distinct from those of eastern Africa, and are, generally, in disagreement. The question of the occurrence of the AHP in **southern Africa** is still unclear; here, southern Africa is all sites south of 15°S (Fig. 2). Publications considering the AHP in southern Africa have included sites as far as 25°S, and the results from these sites again do not resemble those in other regions (Burrough and Thomas, 2013).

More recently published research has identified records of the AHP in **equatorial Africa**. Most, if not all, equatorial Africa sites fall within the bounds of the Inter-Tropical Convergence Zone, an east-west low-pressure region near the equator where surfaces northeasterly and southeasterly trade winds meet (Yan 2005), and the Congo Air Boundary, a convergence over equatorial Africa that separates the Atlantic and Indian Ocean air masses (e.g., Russell et al., 2003; Foerster et al., 2012; Costa et al., 2014; Forman et al., 2014; Junginger et al., 2014). Though these sites in equatorial Africa are located near each other, the diversity of vegetation and hydroclimate regimes requires the further distinction of this region into subregions. The site considered in this study, Matupi Cave, lies within **central equatorial Africa**, a rainforest region of equinoctial rainfall. Sites within 15°N and 15°S, and within 15°E and 30°E are in central equatorial Africa (Fig. 2). Sites in **southeastern equatorial Africa** are more temperate and are east of 35°E, and between the equator and 15°S (Fig. 2). Drier still, sites in **northeastern equatorial Africa** are also east of 35°E, but between the equator and 15°N (Fig. 2). The term **eastern equatorial Africa** is also used in this study to describe a region that contains both northeastern equatorial and southeastern equatorial Africa. These regions are referenced again in a later section describing the setting at Matupi Cave.

Figure 3 demonstrates some of the most cited study areas in which the AHP has been recognized and may best exemplify what most researchers consider to be the general geographic extent of the AHP (Willis et al. 2013). This figure similarly defines the regions of Africa and shows the diversity of paleorecord proxies within those regions. Studies out of northern Africa are almost entirely dominated by paleolimnological proxies and pollen records. This is markedly distinct from studies out of western, equatorial, and southern Africa that typically report isotope, pollen, and mixed proxy records.

An increase in rainfall coeval with the AHP has also been identified in records in the tropical Americas (Haug et al., 2001), southeast Asia (Wang et al., 2001; Dykoski et al., 2005), and the Middle East (Fleitmann et al., 2007). The pluvial conditions of the AHP have largely been attributed to an increase in solar insolation at the northern hemisphere mid-latitudes, and therefore these coeval increases in rainfall at similar latitudes are to be expected.

1.2.2. Timing of the African Humid Period

Early publications describing the African Humid Period reported its onset at ca. 9 kyr BP and termination at ca. 6 kyr BP (e.g., et al., 1985), but more recent publications have reported that pluvial conditions existed in Africa ca. 5.5 to 14.8 kyr BP (deMenocal et al., 2000; Shanahan et al., 2015). The onset and termination of the AHP have been described both as synchronous and abrupt (e.g., deMenocal et al., 2000; Tierney et al., 2008), and asynchronous and gradual (e.g. Jung et al., 2004; Kröpelin et al., 2008; Marshall et al., 2011). Costa et al. (2014) points out that climate modelling studies have also reported conflicting views, suggesting an abrupt onset and termination in their western Africa, and

a gradual onset and termination in their eastern Africa (Hély et al., 2009). The decline of the AHP in southeastern equatorial Africa has also been described as an abrupt collapse in vegetation followed by a gradual precipitation decline (Liu et al., 2007).

Two publications have remarked on the two-pulsed nature of the AHP, though they suggest different timing for those pulses. Holmes and Hoelzmann (2017) have identified two pulses in northern Africa at 8 to 10.5 kyr BP and 4.5 to 7.5 kyr BP that correlate well with publications noting the major lacustrine phases of the Sahara (Gasse et al., 2002). Conversely, Liu et al. (2017) have identified two pulses in southeastern equatorial Africa at 8 to 10 kyr BP and 5.5 to 8 kyr BP. These pulses are not coeval and likely reflect real differences in the regional expression of the AHP.

1.2.3. Causes of the African Humid Period

Both early and recent publications agree that increased solar insolation in the north African subtropics during the boreal summer season resulted in enhanced transport of water vapor from the Atlantic Ocean onto land, and therefore caused a sudden increase in rainfall. Accompanied by land surface albedo feedbacks associated with changes in vegetation, this contributed to the humid conditions observed during the African Humid Period (e.g., Kutzbach and Liu, 1997; deMenocal et al., 2000; Shanahan et al., 2015).

Studies more specific to AHP responses in eastern equatorial Africa have attributed increased humid conditions to changes in Indian Ocean sea surface temperatures, feedbacks between the monsoons and coastal upwelling intensity, and migration of the ITCZ and the CAB (Adkins et al. 2006; Tierney et al. 2008; Liu et al. 2017). A recent study by Liu et al. (2017) reconstructs the AHP from a geochemical record of a near-shore

sediment core off Tanzania and provides a high-resolution record of AHP drivers specific to southeastern equatorial Africa. As stated earlier, Liu et al. (2017) found that the AHP in southeastern equatorial Africa after 10 kyr BP was a two-pulsed event (Results prior to 10 kyr BP that would include the onset of the AHP at 14.8 kyr BP were not reported.). The first pulse, AHP I (8 to 10 kyr BP), was likely linked to the elevated Atlantic moisture due to the eastward migration of the CAB. The second pulse, AHP II, (5.5 to 8 kyr BP), was likely linked to the additional moisture from the Indian Ocean due to higher sea surface temperatures. Though the drivers behind both pulses are ultimately linked to increased northern hemisphere insolation, the description provided by Liu et al. (2017) of the AHP should be carefully constrained to southeastern equatorial Africa. This publication is a good example of the differences between northern Africa AHP sites and eastern equatorial Africa AHP sites, which are in increasing disagreement. Studies modelling the past climate of eastern equatorial Africa have also been useful, providing greater insight to the potential drivers of the AHP in the region (Tierney et al., 2011a).

With this considered, high-resolution records of the AHP from central equatorial Africa are nearly non-existent in the literature. Russell et al. (2003) reconstructs the AHP at Lake Edward using lacustrine data and suggests a gradual termination from 4.2–5 kyr BP. The results from this study should, theoretically, align most closely with those of Russell et al. (2003) due to site similarity.

1.3. Study importance

This study is important because it improves our understanding of the African Humid Period in central equatorial Africa, a region lacking in AHP records. Only a single

stalagmite study reconstructing the AHP was identified (Wang et al., 2019), and this publication sources from many of the same co-authors who contributed to this study. From a disciplinary standpoint, stalagmite records from equatorial regions and from high latitude sites in Africa are scarce (Wong and Breecker, 2015). This study is a high-resolution, multi-proxy addition that is useful, both in terms of its contribution to stalagmite studies and its contribution to AHP reconstructions.

Figure 1. Stalagmite formation. Figure 1.2 of Voarintsoa (2017) shows the process of stalagmite formation (from dissolution, degassing and/or evaporation of the dripwater to CaCO3 precipitation of stalagmite) and the linkage between the cave, the epikarst, and the landscape above the system. Stalactites and stalagmites are examples of speleothems.

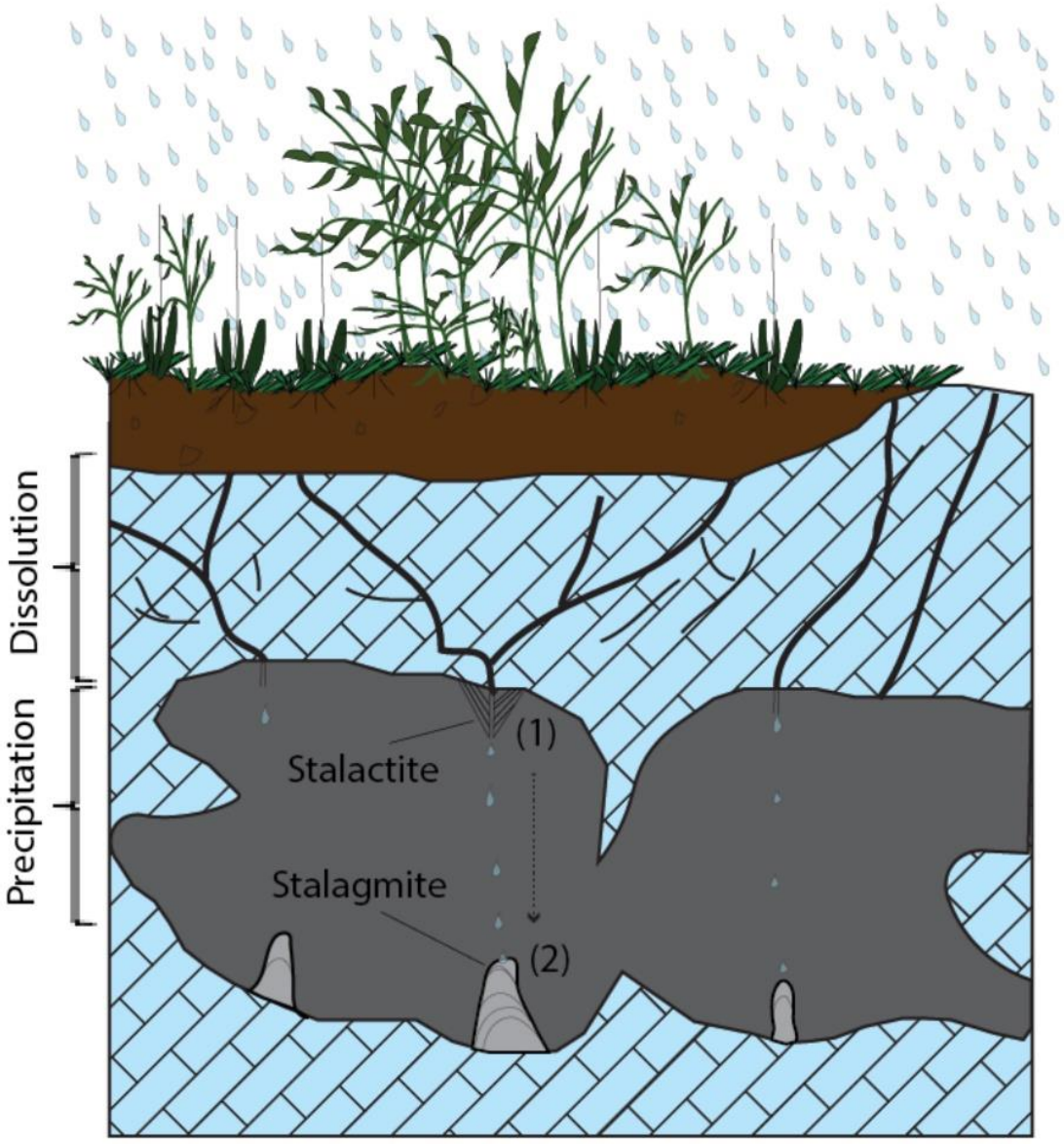

(1): Degassing (and/or evaporation) begins

⋯⋯→ : Saturation state increases

(2): $CaCO_3$ precipitation into stalagmite

Figure 2. Map of regions of Africa using images from the NASA Moderate Resolution Imaging Spectroradiometer (MODIS) program that were obtained in October 2004 as a part of the Blue Marble image series. This map divides the African continent into four hydroclimate regions: northern, western, southern, and equatorial Africa. Here, equatorial Africa is divided into two subregions due to differences in vegetation and hydroclimate seasonality: central equatorial and eastern equatorial. Eastern equatorial is further divided into northeastern equatorial and southeastern equatorial Africa. Matupi Cave, the site discussed in this study, is marked with a red star on the eastern margin of central equatorial Africa.

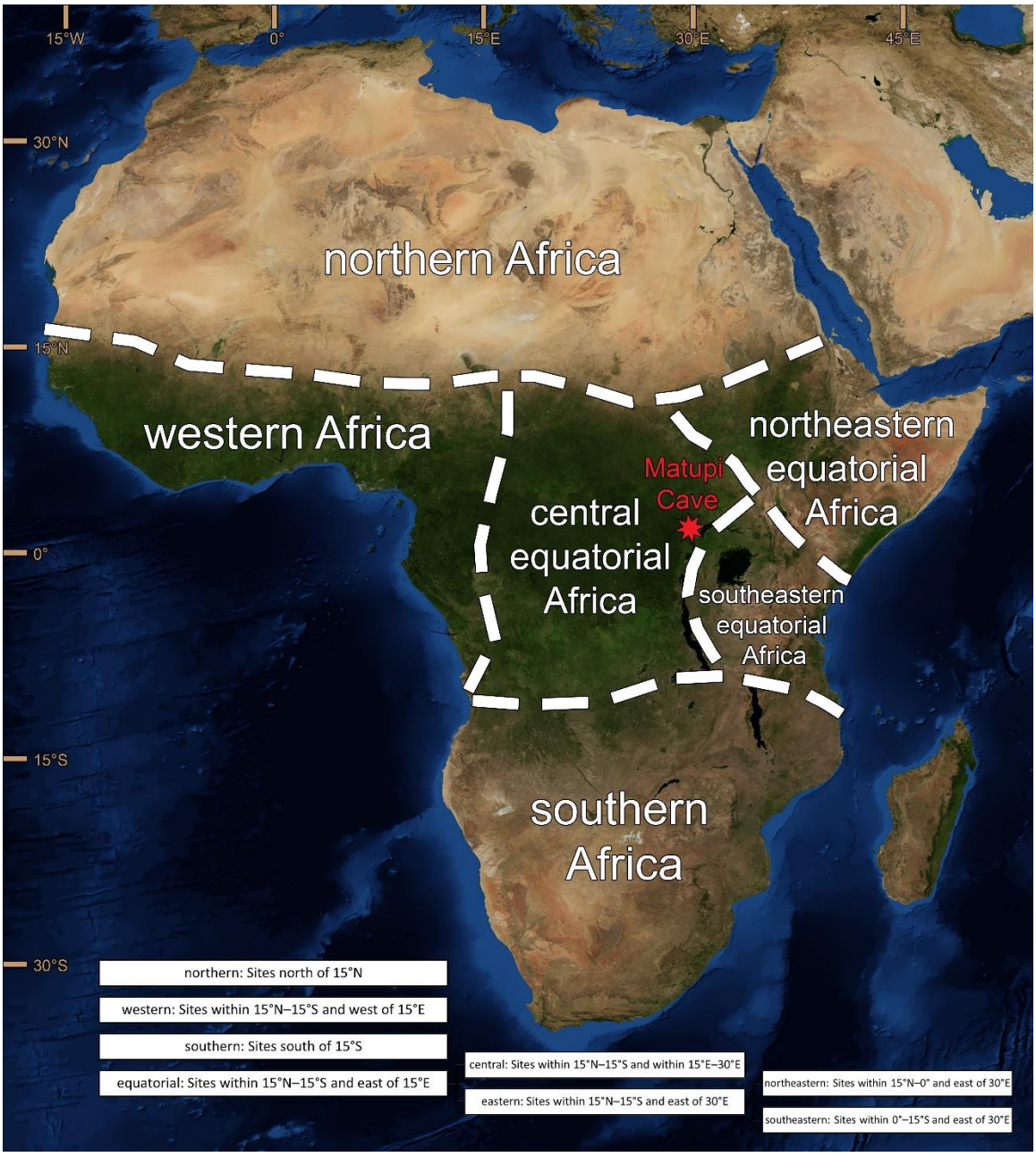
15°W
0°
15°E
30°E
45°E
30°N
15°N
0°
15°S
30°S
northern Africa
western Africa
central equatorial Africa
northeastern equatorial Africa
southeastern equatorial Africa
southern Africa
Matupi Cave
northern: Sites north of 15°N
western: Sites within 15°N–15°S and west of 15°E
southern: Sites south of 15°S
equatorial: Sites within 15°N–15°S and east of 15°E
central: Sites within 15°N–15°S and within 15°E–30°E
eastern: Sites within 15°N–15°S and east of 30°E
northeastern: Sites within 15°N–0° and east of 30°E
southeastern: Sites within 0°–15°S and east of 30°E

Figure 3. Map of commonly cited AHP sites. Adapted Figure 1 from Willis et al. (2013) showing commonly cited AHP terrestrial and near-shore sites in north Africa (Sahara), West Africa, East Africa, and Southern Africa as defined by Seneviratne et al. (2012). These regions are similar, but not equivalent to, the regions defined in this study. Mixed proxies were a combination of pollen, molecular proxies, and/or diatoms. The distinction of squares and circles is not significant in this context. Main bodies of water during the AHP were obtained from Drake et al. (2011). Matupi Cave (1.19°N, 30.01°E), the site discussed in this study, is marked with a white star.

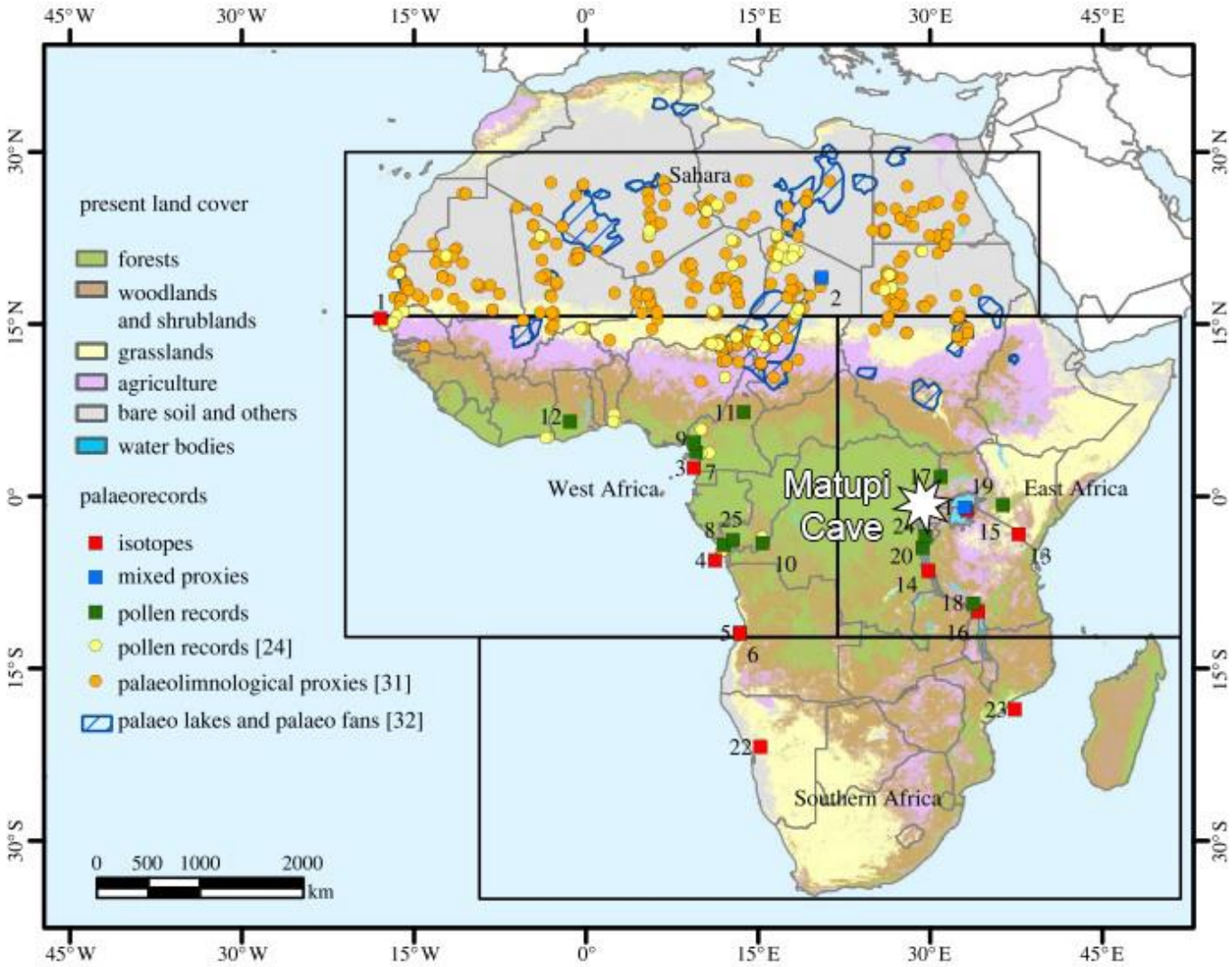
45° W
30° W
15° W
0°
15° E
30° E
45° E
30° N
15° N
0°
15° S
30° S
present land cover
forests
woodlands and shrublands
grasslands
agriculture
bare soil and others
water bodies
palaeorecords
isotopes
mixed proxies
pollen records
pollen records [24]
palaeolimnological proxies [31]
palaeo lakes and palaeo fans [32]
Sahara
West Africa
Matupi Cave
East Africa
Southern Africa
0 500 1000 2000
km

CHAPTER 2: SETTING

2.1. Geography and geology

Matupi Cave (1.19°N, 30.01°E, 1110 m above sea level) is the largest cave of the greater karst system of Mount Hoyo, a mountain located in the Ituri Province in northeastern Democratic Republic of Congo (Fig. 4). Matupi Cave is near some of the province's largest cities, including Irumu (30 km NW), Beni (100 km SW), and the province's capital, Bunia (50 km NE). Mount Hoyo (1450 m above sea level) is a horst bounded on its western side by an escarpment oriented approximately southwest to northeast. Though Mount Hoyo is within the East African Rift with strong evidence of tectonism nearby, its thinly to massively bedded Precambrian limestone show no signs of metamorphism and strata are horizontal (Brook et al. 1990). Mount Hoyo's cave system and nearby Lake Albert and Lake Edward all lie within the northern portion of the western branch of the East African Rift. Other nearby African Humid Period sites are between the rift branches (e.g., Lake Victoria) or within the eastern branch (e.g., Lake Suguta).

2.2. Vegetation

The position of Matupi Cave in central equatorial Africa and within the Ituri rainforest controls its modern climate. In the Köppen-Geiger classification system (Beck et al. 2018), Matupi Cave grades between tropical monsoon (Am, medium blue) and tropical savanna, dry winter (Aw, light blue) (Fig. 5a). In other words, the forested land to the east of Matupi is less dense and less wet (Aw) and the forested land to the west of

Matupi is more dense and more wet (Am). Rainforests farther west into the Congo River Basin are the wettest in the region and are classified as tropical rainforest (Af, dark blue). Matupi Cave's position on that eastern edge of the Congo River Basin and its proximity to the equator make it a biodiverse tropical site. Brook et al. (1990) succinctly describes Matupi Cave as "a drier type of species-rich equatorial rainforest", bounded by savanna woodland in the east and a wetter type of equatorial rainforest on the west. The other AHP site in central equatorial Africa, Lake Edward, is also classified as tropical savanna, dry winter (Aw).

The classifications of AHP sites in the remaining subregions of eastern equatorial Africa are remarkably different from those of central equatorial Africa. Sites in southeastern equatorial Africa such as Lake Naivasha, Mt. Kilimanjaro, and Lake Challa are drier, with more temperate classifications (Csb, Cwb, and Cfb respectively). Northeastern equatorial Africa sites are drier still, where Lake Turkana and Lake Suguta are both classified as arid hot steppe (BSh). The most extreme site of the Chew Bahir Basin in northeastern equatorial Africa grades into the same conditions of the Sahara in northern Africa with the driest classification of arid hot desert (Bwh). The heterogeneity of equatorial Africa vegetation zones requires the aforementioned subregions. This is particularly important when considering AHP sites that, while in close proximity, are in actuality dissimilar and, in some cases, completely inverse (e.g., Af tropical rainforest of the Congo River Basin and Bwh arid hot desert of the Chew Bahir Basin).

2.3. Climate

The climatic data of Harris et al. (2014) presented on the World Bank Group's website (climateknowledgeportal.worldbank.org) indicate Matupi Cave has a mean annual temperature of approximately 23°C with little variation throughout the year (Fig. 5c). Rainfall, however, varies greatly throughout the year and is dependent on the location of the tropical rain belt. Mean annual rainfall at Matupi is approximately 1186 mm and is characterized by two rainy seasons: A strong rainy season in September–November, and a weaker rainy season in March–May (Fig. 5d). Both rainy seasons begin during the equinoxes (September and March), and the months following the equinoxes (October and April) are the wettest for their respective season. The two rainy seasons are separated by dry intervals, the more severe of which is from December to February. This rainfall pattern is distinct from other AHP sites in equatorial Africa, where many sites in southeastern equatorial Africa experience intense rainfall in December–February (e.g., sites described in Tierney et al., 2011a) and many sites in northeastern equatorial Africa are dry year-round. With that said, it is still possible to identify sites in eastern equatorial Africa with equinoctial rainfall patterns like that of Matupi Cave (e.g., sites 9–12 in Fig. 6).

As stated earlier, the rainfall patterns at Matupi Cave are controlled by the migration of the tropical rain belt (Fig. 5b). This migration is controlled, at least in part, by the heating and upward movement of air driven by changes in insolation. The resulting two rainy seasons in March–May and September–November follow the annual maxima in insolation at Matupi Cave in February/March and September respectively (Fig. 5e). Likewise, to the north is a region of summer rainfall coincident with or following maximum insolation in June to August, and to the south is a region of summer rainfall coincident with

or following maximum insolation in December to February (Fig. 6), further supporting the notion that maximum insolation is associated with tropical rain belt migration which causes the onset of the rainy seasons.

Figure 4. Map of Matupi Cave site location. **(**A) Image of Africa. This image, and those in B and C, are from the NASA Moderate Resolution Imaging Spectroradiometer (MODIS) program and were obtained in October 2004 as a part of the Blue Marble image series. (B) A map of part of equatorial Africa marking Matupi Cave, the site discussed in this study, with a large red star in central equatorial Africa. Other eastern Africa AHP sites discussed in this study are marked and numbered with white circles. (C) A map of the region surrounding Matupi Cave in northeastern Democratic Republic of Congo. Nearby cities and geographical features are marked with gold circles, and two other AHP sites, Lake Edward and Lake Victoria, are marked with white circles.

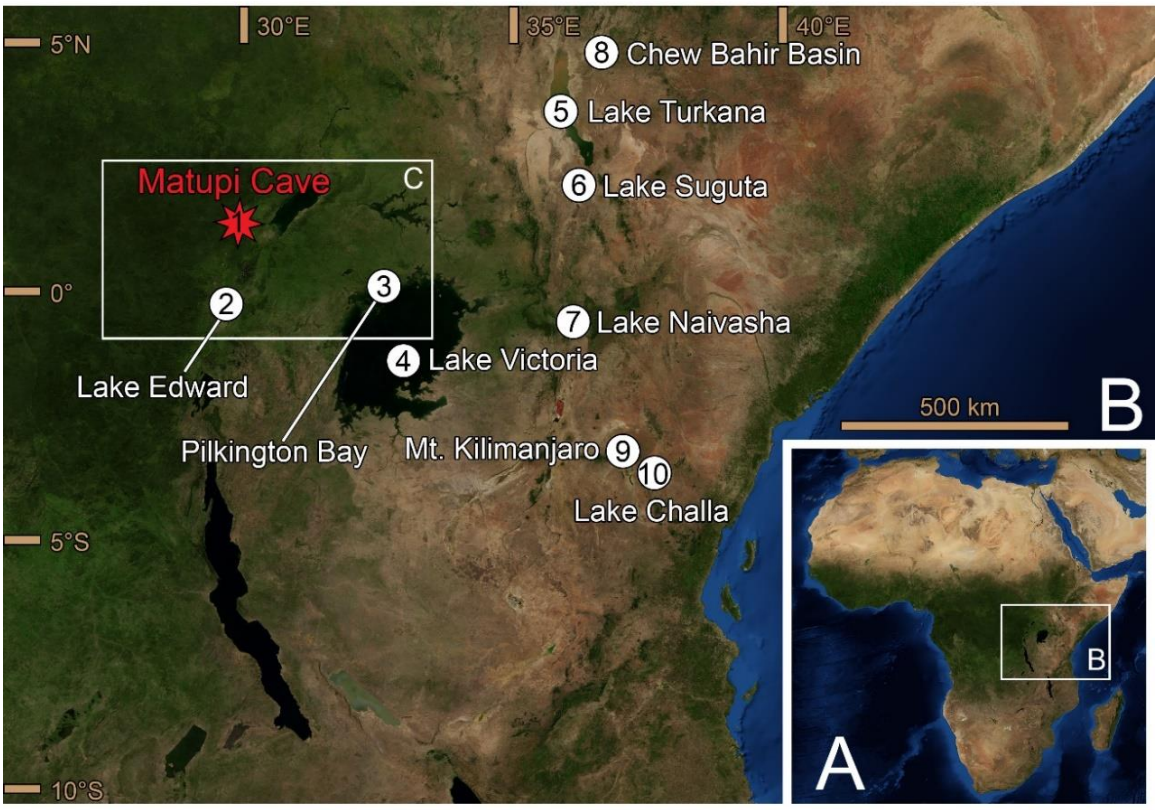
30°E
35°E
40°E
5°N
0°
5°S
10°S
8 Chew Bahir Basin
5 Lake Turkana
6 Lake Suguta
Matupi Cave
C
1
2
3
7 Lake Naivasha
4 Lake Victoria
Lake Edward
Pilkington Bay
Mt. Kilimanjaro
9
10
Lake Challa
500 km
B
A
B

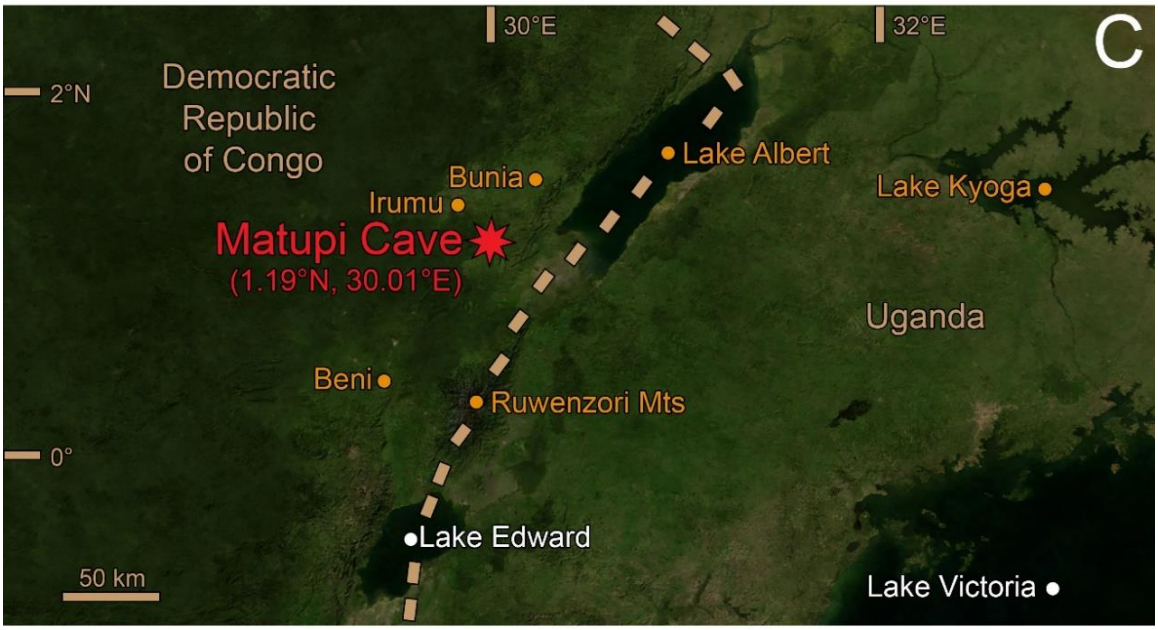
30°E
32°E
2°N
0°
C
Democratic
Republic
of Congo
Lake Albert
Bunia
Irumu
Lake Kyoga
Matupi Cave
(1.19°N, 30.01°E)
Uganda
Beni
Ruwenzori Mts
Lake Edward
50 km
Lake Victoria

Figure 5. Climate of Matupi Cave. (A) A map of Africa showing the Köppen-Geiger climate classification system regions. Matupi Cave is marked in central equatorial Africa as a site that grades between tropical monsoon (Am) and tropical savannah (Aw). (B) Adapted Figure 1. from Tierney et al. 2011 showing seasonal precipitation and wind movement in Africa, with the Intertropical Convergence zone marked with a solid black line and the Congo Air Boundary marked with a dotted black line. Matupi Cave is marked with a red star. (C) A histogram of monthly temperature (°C) at Matupi Cave, DRC. (D) A histogram of monthly rainfall (mm) at Matupi Cave, DRC. (E) A histogram of monthly insolation (W/m^2) at Matupi Cave, DRC.

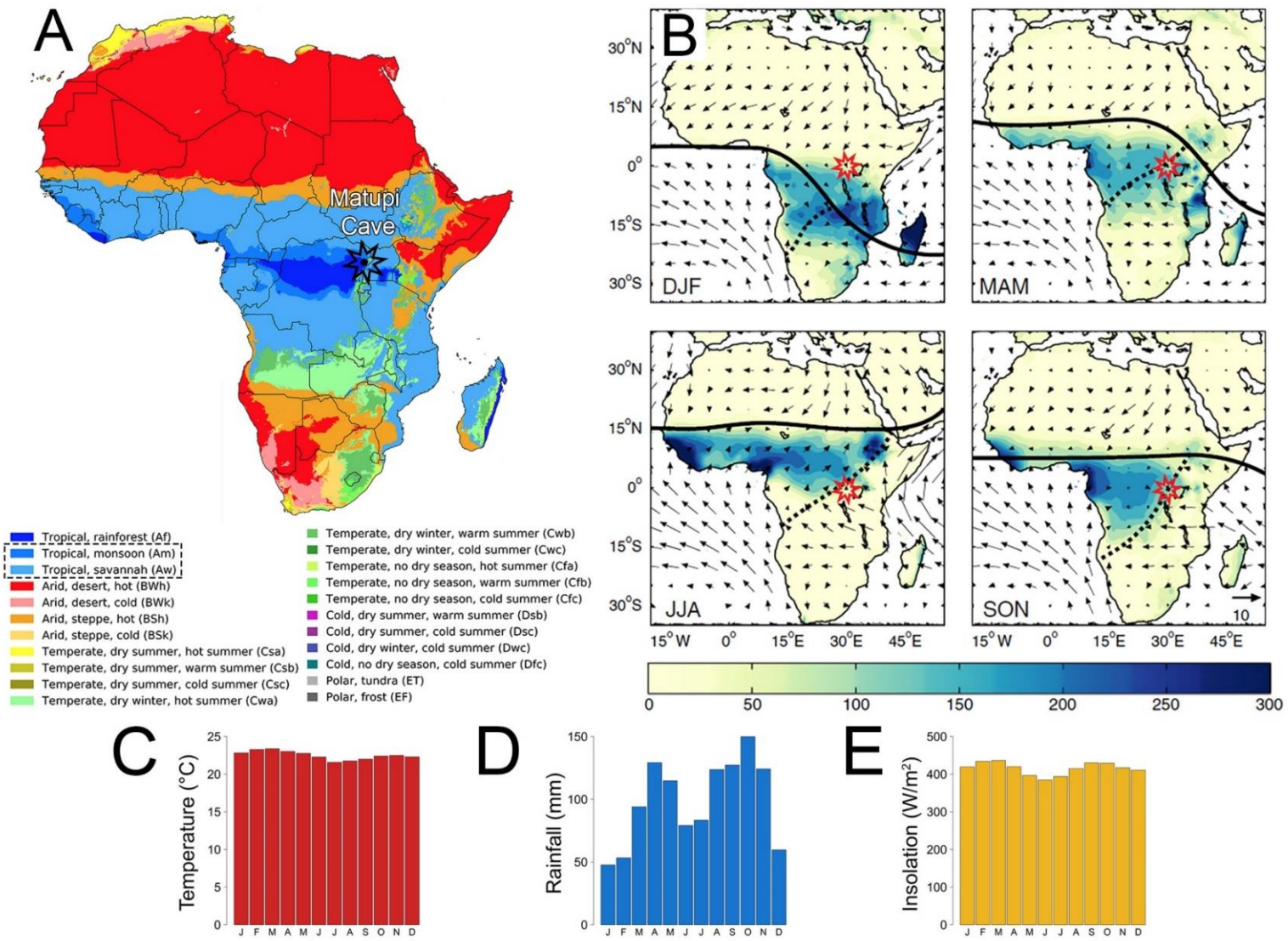
A
Matupi Cave
Tropical, rainforest (Af)
Tropical, monsoon (Am)
Tropical, savannah (Aw)
Arid, desert, hot (BWh)
Arid, desert, cold (BWk)
Arid, steppe, hot (BSh)
Arid, steppe, cold (BSk)
Temperate, dry summer, hot summer (Csa)
Temperate, dry summer, warm summer (Csb)
Temperate, dry summer, cold summer (Csc)
Temperate, dry winter, hot summer (Cwa)
Temperate, dry winter, warm summer (Cwb)
Temperate, dry winter, cold summer (Cwc)
Temperate, no dry season, hot summer (Cfa)
Temperate, no dry season, warm summer (Cfb)
Temperate, no dry season, cold summer (Cfc)
Cold, dry summer, warm summer (Dsb)
Cold, dry summer, cold summer (Dsc)
Cold, dry winter, cold summer (Dwc)
Cold, no dry season, cold summer (Dfc)
Polar, tundra (ET)
Polar, frost (EF)
B
30°N
15°N
0°
15°S
30°S
DJF
MAM
JJA
SON
15°W
0°
15°E
30°E
45°E
0
50
100
150
200
250
300
C
Temperature (°C)
D
Rainfall (mm)
E
Insolation (W/m²)
J F M A M J J A S O N D

Figure 6. Rainfall and insolation in Africa. Rainfall and insolation at Matupi Cave within the greater framework of tropical rain belt migration in Africa. (A) Satellite imagery marking selected sites. (B) Rainfall distribution map, where Matupi Cave is marked as site 4. (C) Histograms of average monthly rainfall in mm for each site, where sites with equinoctial rainfall are marked in red and sites with summer rainfall are marked in gold. (D) Monthly insolation patterns by latitude.

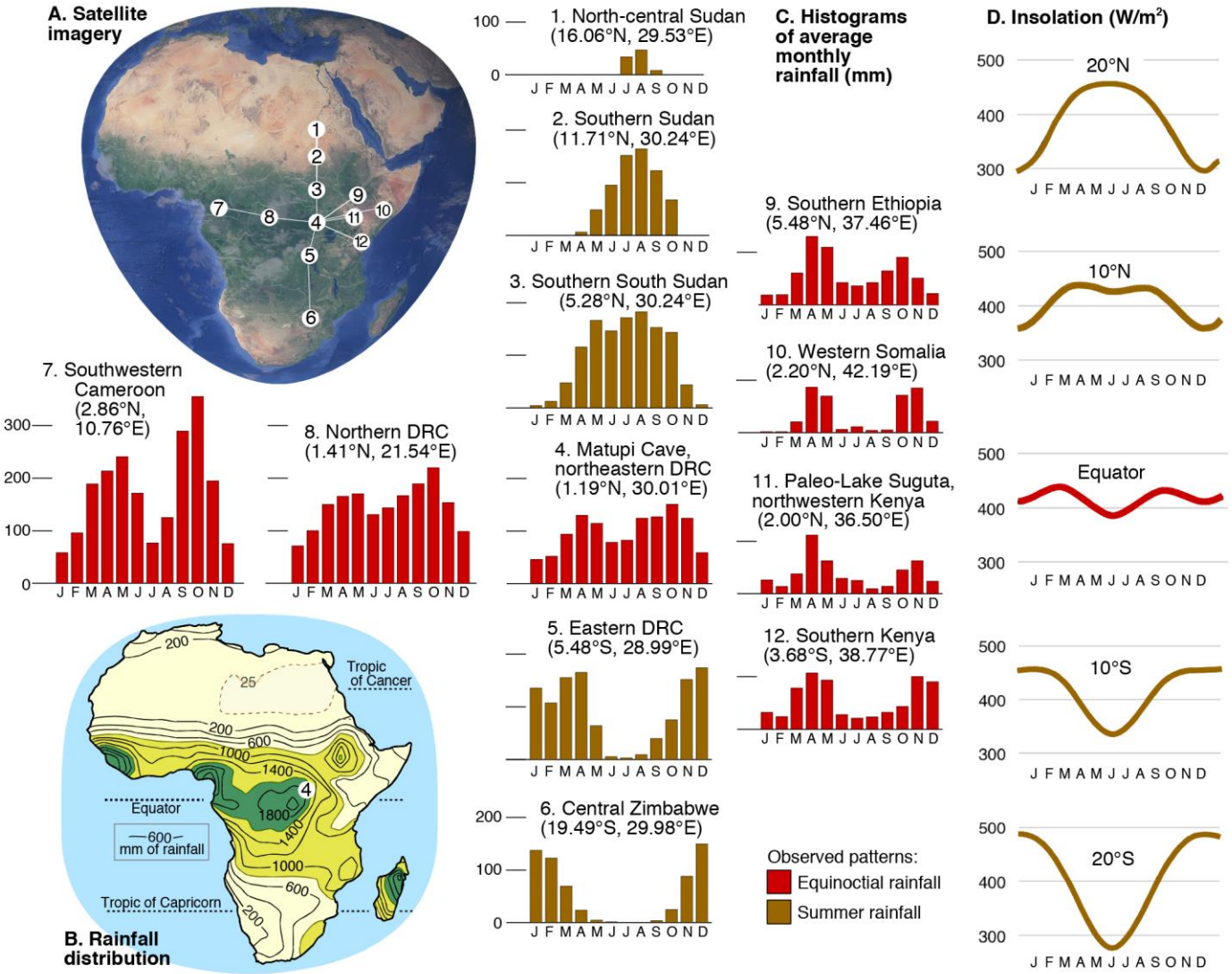
A. Satellite imagery
1
2
3
4
5
6
7
8
9
10
11
12
B. Rainfall distribution
200
25
200
600
1000
1400
1800
Tropic of Cancer
Equator
600
mm of rainfall
Tropic of Capricorn
1. North-central Sudan (16.06°N, 29.53°E)
2. Southern Sudan (11.71°N, 30.24°E)
3. Southern South Sudan (5.28°N, 30.24°E)
4. Matupi Cave, northeastern DRC (1.19°N, 30.01°E)
5. Eastern DRC (5.48°S, 28.99°E)
6. Central Zimbabwe (19.49°S, 29.98°E)
7. Southwestern Cameroon (2.86°N, 10.76°E)
8. Northern DRC (1.41°N, 21.54°E)
J F M A M J J A S O N D
C. Histograms of average monthly rainfall (mm)
9. Southern Ethiopia (5.48°N, 37.46°E)
10. Western Somalia (2.20°N, 42.19°E)
11. Paleo-Lake Suguta, northwestern Kenya (2.00°N, 36.50°E)
12. Southern Kenya (3.68°S, 38.77°E)
Observed patterns:
Equinoctial rainfall
Summer rainfall
D. Insolation (W/m²)
20°N
10°N
Equator
10°S
20°S

CHAPTER 3: METHODS AND MATERIALS

3.1. Specimen collection and preparation

Stalagmite MAT-12 was collected from Matupi Cave, DRC in 1987 by Dr. George A. Brook. Stalagmite MAT-12 is a section of an originally 80 cm long stalagmite, and specifically the interval from approximately 40 to 68 cm above the base. Stalagmite MAT-12 was collected from a room at least 30 m within the cave (Fig. 7). Upon collection, the specimen showed no evidence of re-solution apparent in some specimens collected during the same field season (Brook et al., 1990).

After collection, Stalagmite MAT-12 was halved and polished prior to radiometric-age sampling, stable-isotope sampling, and pollen residue extraction described in Brook et al. (1990). The stalagmite was later resampled in various phases for radiometric ages and stable isotopes, and those results are reported herein. The radiometric ages and stable isotope data reported in Brook et al. (1990) are omitted from this work due to their broad analytical error. Prior sampling also utilized various lower-resolution indexing systems. During resampling, Stalagmite MAT-12 was assigned a new indexing system by scanning the polished face and using a high-quality .tiff image in Adobe Photoshop to assign measurements along the central axis. This indexing system allowed for consistency in sampling and was required for determining the distance from the top of the stalagmite.

3.2. Radiometric analysis

Twenty-four samples were drilled from Stalagmite MAT-12 for U-Th radiometric analysis. Sampling was completed in two phases in July 2014 and February 2019 by Dr. Ny Riavo G. Voarintsoa and Dr. L. Bruce Railsback. Sample drilling was conducted using a hand-held dental drill equipped with a carbide round tip bur (Bur U.S. No. 4) to trace specific layers to produce U-Th sample trenches approximately 2 mm wide. Great caution was taken to avoid drilling into dark detrital layers or across layer-bounding surfaces (Railsback et al., 2013). Dating samples weighed between 100 and 250 mg and were transferred to flat-bottomed glass vials.

U-Th age samples were processed on a multi-collector inductively coupled plasma mass spectrometer (MC-ICPMS) at the Minnesota Isotope Laboratory at the University of Minnesota following the analytical methods and chemical separation methods of Shen et al. (2002) and Cheng et al. (2013). Analysis was completed in three phases in August 2014, December 2014, and August 2019 by Dr. Fuyuan Liang, Dr. Hai Cheng, and Dr. R. Lawrence Edwards. Corrected ^{230}Th ages assume an initial ^{230}Th/^{232}Th atomic ratio of 4.4 ± 2.2 x 10^{-6}, which is the value for a material at secular equilibrium with the bulk earth ^{232}Th/^{238}U value of 3.8.

3.3. Petrographic analysis

Stalagmite MAT-12 was examined in hand sample for the presence of layer-bounding surfaces known as Type E and Type L surfaces (Railsback et al., 2013). Type E layer-bounding surfaces are surfaces at which layers have been truncated or eroded at the crest of a stalagmite and can be identified by irregular terminations, dissolutional cavities,

and detrital coatings. Type L layer-bounding surfaces are surfaces below which layers become thinner upward and or/layers have lesser lateral extent upward and can be identified by decreased layer-specific width. Type E surfaces generally indicate dissolutional erosion due to wetter conditions, and Type L surfaces generally indicate lessened deposition due to drier conditions. The inclusion of layer-bounding surface data strengthens paleoclimate interpretations made from the stable isotope data and aids the construction of the age model in that it improves the visibility of hiatuses, or periods of non-deposition. Here, layer-bounding surfaces were only identified in hand sample, though thin section analysis may also be utilized when layer-bounding surfaces are not apparent in hand sample. The surfaces identified herein were easily seen under bright laboratory lights and with the occasional aid of a magnifying lens. All layer-bounding surfaces were identified and recorded by Dupont and Railsback in September 2019.

Fifteen non-contiguous samples were drilled from Stalagmite MAT-12 for X-ray diffraction (XRD) mineralogical analysis, producing sample trenches approximately with a vertical extent of 3 mm (Bur U.S. No. 8). Samples weighed approximately 5 mg and were stored in glass cylindrical vials. Prior to analysis, each sample was packed into a rounded glass microscope slide that was cleaned using compressed air and Kim Wipes between samples. Samples were analyzed using CoKα radiation on the Bruker D8 X-ray Diffractometer in the Department of Geology at the University of Georgia by Dupont and Railsback in January and February 2020. The diffraction angle 2Θ was set to a range of 20 to 60°. XRD data was processed in EVA to measure peak areas of calcite and aragonite for each sample. These peak areas were expressed as a ratio of aragonite area over total area (A_{111} / A_{111} + C_{1040}) and converted to percent aragonite.

Stalagmite MAT-12 was also examined to measure layer-specific width throughout the specimen. Layer-specific width is the horizontal distance between two points of the flanks of any single stalagmite layer (e.g., Fig. 2 of Sletten et al. 2013, Fig. 3 of Railsback et al. 2014). Layer-specific width generally changes throughout a stalagmite, and here serves as another source of paleoclimate data, with smaller widths indicating drier conditions and greater widths indicating wetter conditions. To determine layer-specific width, easily visible layers of the growth axis of MAT-12 were identified from a high quality .jpeg image scan opened in Adobe Photoshop. After determining the top of the layer, measurements were taken at an appropriate but equidistant spacing below the crest of each layer, here called 'drop-down distance'. This drop-down distance method was easier to complete, and just as accurate as earlier methods described by Sletten et al. (2013), which involved using a set angle rather than a set drop-down distance to determine each measurement. The methods of Sletten et al. (2013) were more time consuming, and therefore this new drop-down distance method is recommended for future layer-specific width measurements. To avoid bias in layer choice and selection of an appropriate drop-down distance, Dupont and Railsback both took several layer-specific width measurements independently in January 2020. A total of 35 measurements were recorded, where Railsback selected 16 layers and measured from a drop-down distance of 6 mm, and Dupont selected 19 layers and measured from a drop-down distance of 5 mm.

3.4. Stable isotope analysis

One hundred forty-two samples were drilled from Stalagmite MAT-12 for carbon ($\delta^{13}C$) and oxygen ($\delta^{18}O$) stable isotope analysis. Sampling was completed in one phase in

June 2019 by Dupont. Samples were drilled individually to employ a continuous sampling strategy along the growth axis of the stalagmite that produced trenches approximately 0.5 mm wide (Bur U.S. No. ¼). Samples were regularly spaced at an interval of 2.5 mm to produce approximately 50-100 µg of powdered $CaCO_3$ and transferred into 4.5 mL Labco exetainers. This sampling approach was selected after an age model for Stalagmite MAT-12 was constructed to yield stable isotope samples that were of an appropriate resolution for the paleoclimate trends in question. In other words, this strategy opted for stable isotope samples that report trends from approximately five years as opposed to higher resolution samples that would report trends on a yearly basis.

The samples were processed in June 2019 on a GasBench isotope ratio mass spectrometer (IRMS) at the Alabama Stable Isotope Laboratory at the University of Alabama following the analytical methods of Paul and Skrzypek (2007), Skrzypek and Paul (2006), and Lambert and Aharon (2011). Internal standards NBS19 ($\delta^{13}C$ = +1.95, $\delta^{18}O$ = –2.2 ‰ relative to VPDB) and IAEA-603 ($\delta^{13}C$ = +2.46, $\delta^{18}O$ = –2.37 ‰ relative to VPDB) were analyzed with a 2-sigma error of ±0.1 ‰ for both $\delta^{13}C$ and $\delta^{18}O$. Both standards were reported in per mil (‰) relative to Vienna PeeDee Belemnite (VPDB), and the results were standardized relative to NBS19. The ratios reported here ($^{13}C/^{12}C$ and $^{18}O/^{16}O$) are expressed in delta notation: $\delta_x = [(R_{sample} - R_{standard}/R_{standard}] * 1000$ (where x is ^{13}C or ^{18}O and R is the ratio). To correct for fractionation between aragonite and calcite, the isotope ratios of aragonitic samples were transformed to a calcite basis by a subtraction of 1.7‰ for $\delta^{13}C$ (Romanek et al., 1992) and 0.8‰ for $\delta^{18}O$ (Kim et al., 2007) respectively. This transformation was necessary to ensure that aragonitic ratios are comparable to calcitic ratios.

Figure 7. Map of Matupi Cave interior. Map is in plan view. The original figure was produced upon the cave survey by R. Michel and E. Poty in 1974 and published in French (source unknown). The figure was later modified by G. Brook in 1988 and published in Brook et al. (1990) to include the location of various Matupi stalagmites. Now modified by L. Dupont in 2021, large red stars mark the location of Stalagmites MAT-12 and MAT-23 and various French phrases have been translated, where French “salle” is translated as English “room” and French “chantoir” is loosely translated as English “cave opening”.

Matupi Cave, Mont Hoyo
Democratic Republic of Congo

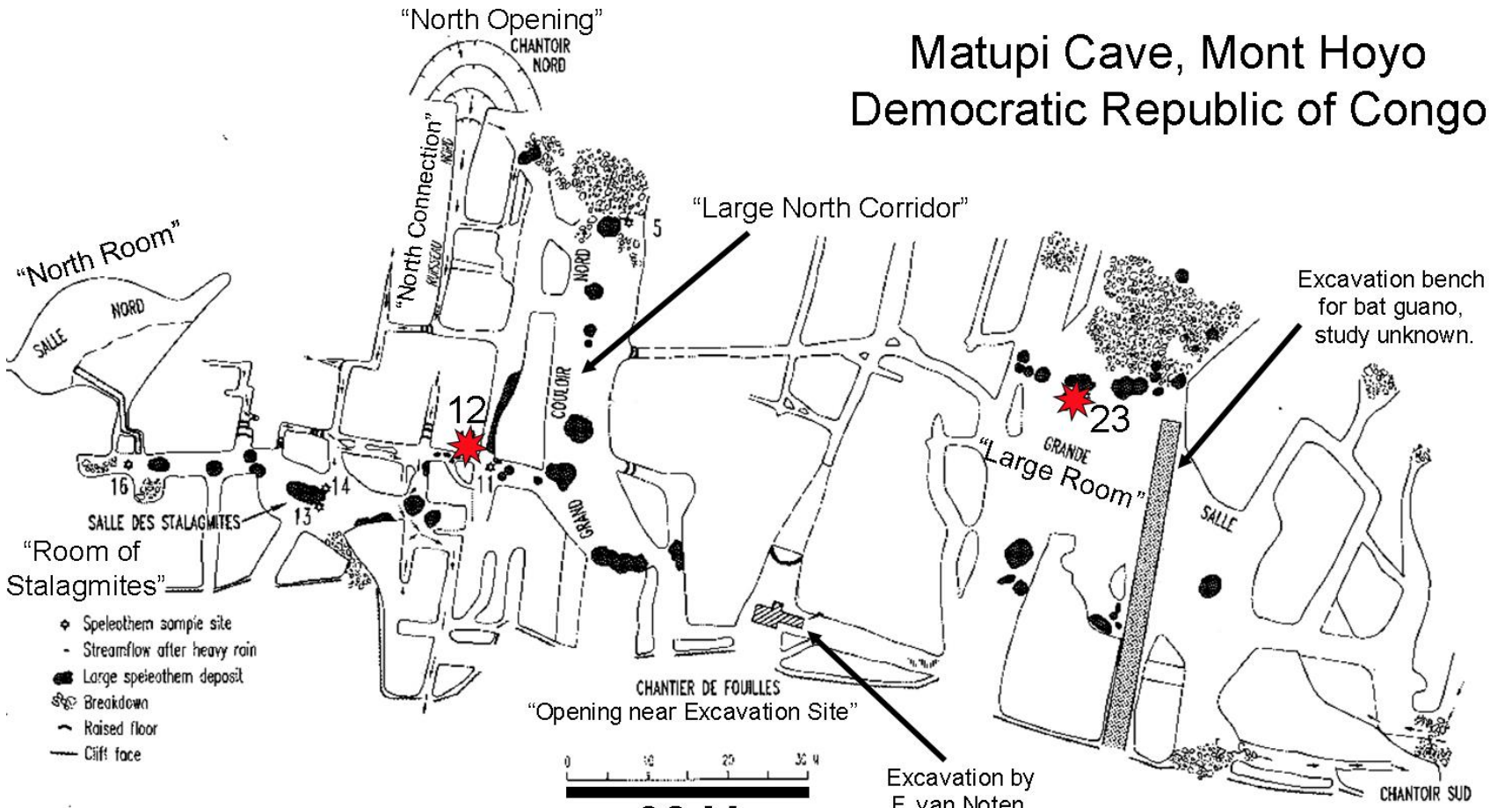

Original survey by R. Michel and E. Poty, 1974. Modified by G. Brook, 1988 and L. Dupont, 2021.

North

CHAPTER 4: RESULTS

4.1. Specimen and layer morphology

Stalagmite MAT-12 is 26 cm tall and has an irregular shape. The main axis of the stalagmite approximates a candlestick morphology, with slight deviations from the vertical growth axis throughout. A secondary axis sits adjacent to the main axis on the left flank of the specimen. These left-flank layers are the left edge of layers that precipitated on top of the main axis of the specimen in the uppermost portion of the stalagmite that was lost during collection. Here, an indexing system has been developed to include the left flank of MAT-12 to extend the record as much as possible (Fig. 8a). This indexing system considers the 'top' layer of the stalagmite to be on the far left of the left flank of Stalagmite MAT-12. Though these far-left layers allowed the extension of the specimen chronology, caution was taken when considering the stable isotope data from these layers due to potential kinetic fractionation at the extent of a growth layer (Hendy 1971). The indexing system accounts for 336 mm of potential sample trajectory, where the left-flank layers are from 0–77.5 mm and the main axis layers are from 77.6–336 mm.

Layer-bounding surfaces are common throughout Stalagmite MAT-12, with eight Type L surfaces and two Type E surfaces identified on the main axis and the left flank (Table S1). The Type E surfaces identified are distinctive in that they both overlie Type L surfaces. Those 10 layer-bounding-surfaces were used to guide the construction of the age model by identifying hiatuses (Fig. 9).

4.2. Radiometric age data, age model, and growth rate

Of the 24 U-Th dating samples drilled from Stalagmite MAT-12 (Table 2), 19 samples were used to construct a linear-interpolated age model in conjunction with the layer-bounding surfaces reported above (Fig. 9). Sample age uncertainties range from ±18 yr BP to ±126 yr BP, with an average uncertainty of ±41 yr BP. Two samples, MAT12-001-235 and MAT12-001-167, were resampled due to large uncertainties (±250 yr BP and ±403 yr BP) and are omitted from the age model. The large uncertainty (±403 yr BP) of the age from sample MAT12-001-167 was likely caused by detrital content present in the layer as indicated by the high concentration of ^{232}Th in the sample (Table 2). Three samples, MAT12-001-167R, MAT12-001-115, and MAT12-006-U095 were rejected because they were not consistent with the trend of the other ages but are plotted on the age model in grey. The age model that results from the 19 accepted ages and 10 layer-bounding surfaces reveals that Stalagmite MAT-12 was deposited from 8034 yr BP to 6618 yr BP, with several brief hiatuses throughout. These hiatuses range from 20 years to 90 years. One Type L surface at 127 mm had no impact on the chronology.

This age model allowed for growth rate from the main axis to be reconstructed through time (Fig. 8b, Table S2). The growth rate is intermediate at the bottom of the stalagmite (0.416 mm/yr) until a dramatic drop at 283 mm from top (0.340 mm/yr). Growth rate then returns to an intermediate rate (0.380 mm/yr) before a dramatic increase at 174 mm from top (0.536 mm/yr). Growth rate remains high up to 85 mm from top (0.555 mm/yr). Growth rate measurements after 85 mm from top were not considered as they account for the growth of the left flank of Stalagmite MAT-12.

4.3. Petrography and mineralogy

XRD results indicate that the mineralogy throughout Stalagmite MAT-12, including the left flank, varies and does not follow any trends visible in hand-sample. Ideally, XRD samples can be used to draw connections between the mineralogy of the sample and the appearance of the growth layer from which it was taken. If the appearance of growth layers can make a meaningful connection to the XRD results, then mineralogy can be easily reconstructed by using those features to identify changes in mineralogy throughout the stalagmite. In the case of Stalagmite MAT-12, XRD samples did not reveal any relationship between mineralogy of a layer and its appearance. This resulted in a linear-interpolation approach between the XRD samples to define the mineralogy of the stalagmite as the ideal method and the sampling of each individual growth layer were not possible. These results are expressed as percent aragonite, where 0% is completely calcite and 100% is completely aragonite. Percent aragonite varies throughout Stalagmite MAT-12, with a pure aragonite sample at the base, followed by a large zone of calcite near the bottom of the stalagmite (approximately 272–301 mm from top), followed by a zone of fluctuation between near pure aragonite and 50% aragonite (approximately 155–260 mm from top), and ending with a zone of near pure aragonite at the top of the stalagmite (Fig. 8c, Fig. 10, Table S3).

The 16 layer-specific width measurements recorded by Railsback and the 19 layer-specific width measurements recorded by Dupont show the same trend (Fig. 8d, Table S4). In both cases, layer-specific width was greatest near the bottom of the stalagmite (approximately 270 mm from top) and gradually decreased up the main axis. No layer-specific width measurements were taken from the left flank of the stalagmite.

4.4. Stable isotope data

Stable isotope data is reported from the entire stalagmite, including the left flank (Table S5), and was corrected as specified in section 3.4.

Values of $\delta^{18}O$ range from –6.8 to –2.5‰ vs. VPDB (Fig. 8e). Values of $\delta^{18}O$ generally increase from the bottom of the stalagmite to the top of the left flank. The smallest value of –6.8‰ occurs at 297 mm from top, and another pronounced low of –6.3‰ occurs at 214.7 mm from top. Values of $\delta^{18}O$ are all greater than –5.0‰ after approximately 175 mm from top.

Values of $\delta^{13}C$ range from –13.9 to –8.7‰ vs. VPDB and increase from the bottom of the stalagmite to the top of the left flank similar to the $\delta^{18}O$ data (Fig. 8f). The smallest value of –13.9‰ that occurs at 214.7 mm from top is correlative to the second pronounced low of the $\delta^{18}O$ data. The $\delta^{13}C$ data values then continue to follow the same increasing trend as the $\delta^{18}O$ data, with $\delta^{13}C$ values consistently greater than approximately –12‰ after approximately 175 mm from top.

Table 1. ^{230}Th dating results from Stalagmite MAT-12. Results with 2σ error.

Dft (mm)	Sample	^{238}U (ppb)	^{232}Th (ppt)	^{230}Th / ^{232}Th (atomic x10-6)	$\delta^{234}U^{a}$ (measured)	^{230}Th / ^{238}U (activity)	^{230}Th Age (yr)	^{230}Th Age (yr)[b]	$\delta^{234}U_{Initial}$[c] (corrected)	^{230}Th Age (yr BP)[d] (corrected)	Accepted/ Rejected[e]
3	MAT12-001-H	465.4 ±2.2	2204 ±44	335 ±7	593.4 ±15.2	0.0963 ±0.0007	6773 ±83	6687 ±102	605 ±16	6618 ±102	A
11	MAT12-001-F	423.6 ±0.5	1023 ±21	663 ±14	567.5 ±1.8	0.0970 ±0.0004	6943 ±30	6898 ±43	579 ±2	6829 ±43	A
48	MAT12-006-U027	2841.2 ±7.3	3645 ±74	1276 ±26	549.2 ±2.7	0.0993 ±0.0003	7198 ±26	7174 ±31	560 ±3	7110 ±31	A
62	MAT12-006-U043	1912.3 ±4.2	478 ±10	6456 ±133	525.7 ±2.1	0.0980 ±0.0004	7212 ±30	7207 ±30	537 ±2	7143 ±30	A
75	MAT12-001-02	1425.0 ±4.1	1121 ±23	2166 ±44	583.6 ±3.0	0.1034 ±0.0003	7333 ±28	7318 ±30	596 ±3	7256 ±30	A
79	MAT12-006-U073	662.0 ±0.7	605 ±13	1850 ±39	570.9 ±2.0	0.1025 ±0.0005	7331 ±35	7314 ±37	583 ±2	7250 ±37	A
89	MAT12-006-U095	1736.7 ±2.3	2247 ±45	1266 ±26	519.3 ±1.8	0.0993 ±0.0003	7347 ±21	7322 ±27	530 ±2	7258 ±27	R2
102	MAT12-001-U028	960.0 ±1.0	848 ±17	1893 ±39	535.4 ±1.7	0.1014 ±0.0003	7425 ±24	7408 ±27	547 ±2	7344 ±27	A
102	MAT12-006-U115	1030.2 ±1.7	1455 ±29	1164 ±23	507.3 ±1.8	0.0997 ±0.0002	7438 ±20	7411 ±27	518 ±2	7347 ±27	A
121	MAT12-001-052	880.3 ±1.0	1920 ±39	785 ±16	552.3 ±1.7	0.1039 ±0.0003	7525 ±27	7484 ±40	564 ±2	7415 ±40	A
140	MAT12-001-U070	1063.2 ±1.2	796 ±16	2226 ±46	516.4 ±1.7	0.1010 ±0.0003	7492 ±22	7478 ±24	527 ±2	7414 ±24	A
165	MAT12-001-U095	1729.2 ±2.3	1558 ±31	1872 ±38	521.9 ±1.8	0.1023 ±0.0002	7559 ±20	7542 ±24	533 ±2	7478 ±24	A
176	MAT12-001-115	2549.6 ±4.0	2454 ±49	1770 ±36	517.2 ±1.8	0.1033 ±0.0002	7663 ±20	7645 ±24	528 ±2	7583 ±24	R2
194	MAT12-001-U123	2099.3 ±3.0	408 ±8	8927 ±186	549.4 ±1.7	0.1053 ±0.0002	7648 ±18	7644 ±18	561 ±2	7580 ±18	A
208.5	MAT12-001-U140	1630.5 ±3.3	1099 ±22	2589 ±52	542.5 ±2.1	0.1058 ±0.0002	7717 ±21	7704 ±23	554 ±2	7640 ±23	A
227	MAT12-001-159	2563.1 ±3.9	1003 ±20	4681 ±95	610.7 ±1.9	0.1111 ±0.0002	7759 ±19	7752 ±20	624 ±2	7688 ±20	A
237	MAT12-001-167	1299.7 ±1.4	49092 ±983	63 ±1	588.3 ±1.8	0.1434 ±0.0003	8408 ±29	7839 ±403	601 ±2	7777 ±403	R1
237	MAT12-001-167R	185.3 ±0.2	271 ±7	1325 ±38	656.8 ±2.3	0.1174 ±0.0016	7975 ±112	7949 ±113	672 ±2	7880 ±113	R2
245	MAT12-001-175	720.9 ±0.8	5768 ±116	234 ±5	608.1 ±1.8	0.1136 ±0.0003	7957 ±25	7813 ±105	622 ±2	7749 ±105	A
272	MAT12-001-200	544.0 ±0.6	5299 ±106	195 ±4	611.3 ±1.9	0.1151 ±0.0003	8044 ±25	7869 ±126	625 ±2	7805 ±126	A
279	MAT12-001-208	1129.8 ±1.3	673 ±14	3180 ±66	634.5 ±1.9	0.1149 ±0.0003	7915 ±23	7904 ±24	649 ±2	7840 ±24	A
306	MAT12-001-235	244.1 ±1.9	1637 ±34	427 ±9	298.7 ±13.9	0.1736 ±0.0015	15559 ±229	15410 ±250	312 ±14	15348 ±250	R1
306	MAT12-001-235R	1450.0 ±1.4	1662 ±33	1643 ±33	597.2 ±1.9	0.1142 ±0.0002	8054 ±19	8033 ±24	611 ±2	7964 ±24	A
324	MAT12-001-255	1577.8 ±1.6	2064 ±41	1444 ±29	588.7 ±1.8	0.1146 ±0.0002	8127 ±19	8103 ±25	602 ±2	8034 ±25	A

[a] $\delta^{234}U = ([^{234}U / ^{238}U]_{activity} - 1) \times 1000$.

[b] Corrected ^{230}Th ages assume the initial ^{230}Th/^{232}Th atomic ratio of 4.4 ±2.2 x10^{-6}. Those are the values for a material at secular equilibrium, with bulk earth 232Th/238U value of 3.8. The errors are arbitrarily assumed to be 50%.

[c] $\delta^{234}U_{initial}$ was calculated based on ^{230}Th age (T), i.e., $\delta^{234}U_{initial} = \delta^{234}U_{measured} \times e^{\lambda 234 \times T}$.

[d] B.P. stands for "Before Present" where the "Present" is defined as the year 1950 A.D.

[e] A= Accepted, R1= Resampled due to large uncertainty (≥250 years), not plotted on age model; R2= Rejected because age is not consistent with the trend of the other ages.

Figure 8. Stalagmite MAT-12 results vs. distance from top (mm). (A) Indexing scan of Stalagmite MAT-12 showing the indexing system and the differentiation between the main axis and the left flank. (B) Growth rate data from the main axis reconstructed from the age model of Stalagmite MAT-12 (Fig. 9) in mm/yr. (C) X-ray diffraction data from the entirety of Stalagmite MAT-12, including the left flank, expressed as percent aragonite. (D) Layer-specific width measurements from the main axis of Stalagmite MAT-12 in mm. (E) $\delta^{18}O$ data from the entirety of Stalagmite MAT-12 vs. VDPB. (F) $\delta^{13}C$ data from the entirety of Stalagmite MAT-12 vs. VPBD.

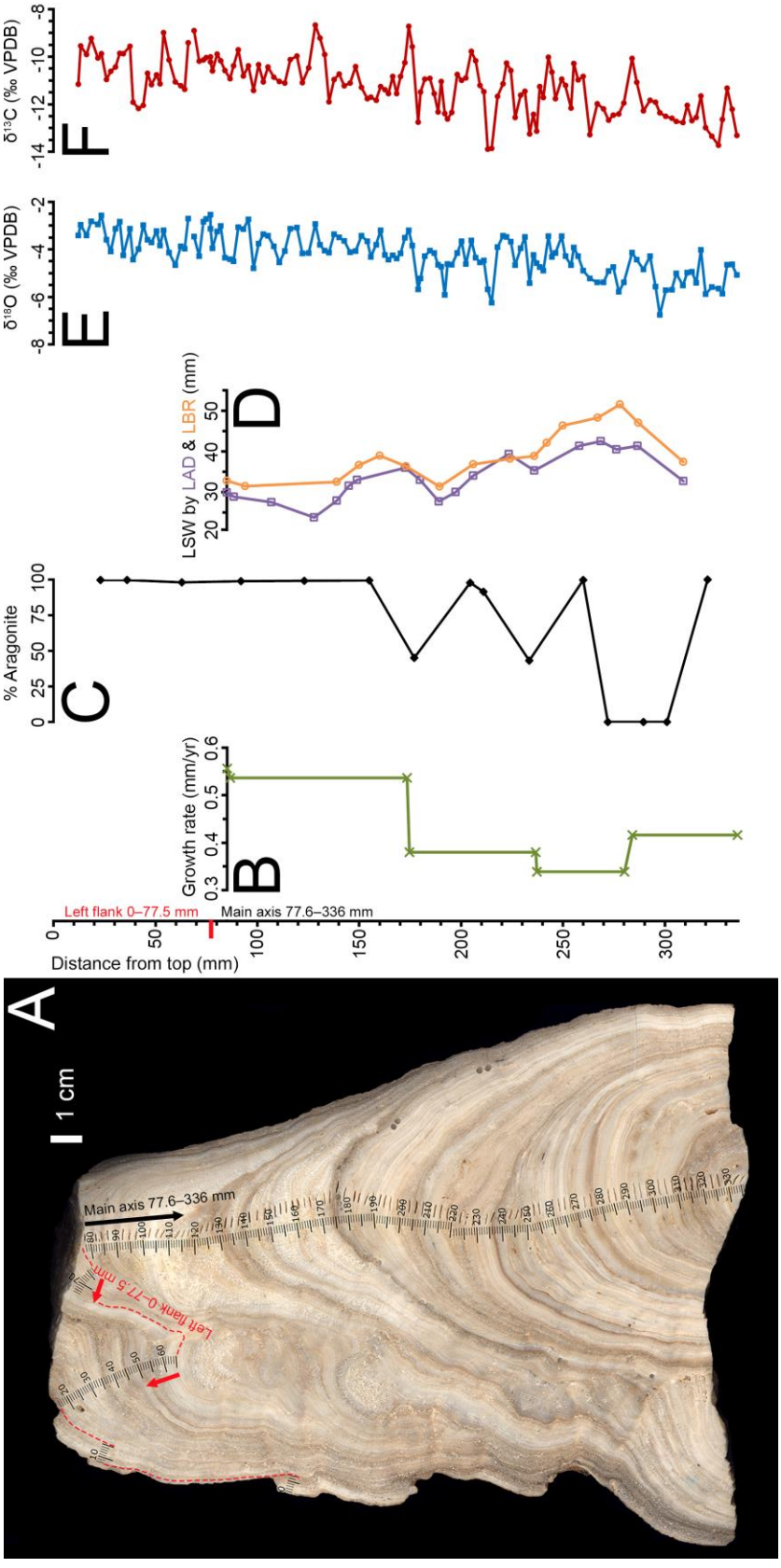
F
δ13C (‰ VPDB)
-8
-10
-12
-14
E
δ18O (‰ VPDB)
-2
-4
-6
-8
D
LSW by LAD & LBR (mm)
20
30
40
50
C
% Aragonite
0
25
50
75
100
B
Growth rate (mm/yr)
0.3
0.4
0.5
0.6
Left flank 0–77.5 mm
Main axis 77.6–336 mm
0
50
100
150
200
250
300
Distance from top (mm)
A
1 cm
Main axis 77.6–336 mm
Left flank 0–77.5 mm

Figure 9. Stalagmite MAT-12 age model. (A) Age model for Stalagmite MAT-12 reconstructed from 18 U-Th dating samples and 10 layer-bounding surfaces. (B) Indexing scan of Stalagmite MAT-12 showing the indexing system in mm. Red arrows from the age model point to the locations of layer-bounding surfaces on the indexing scan.

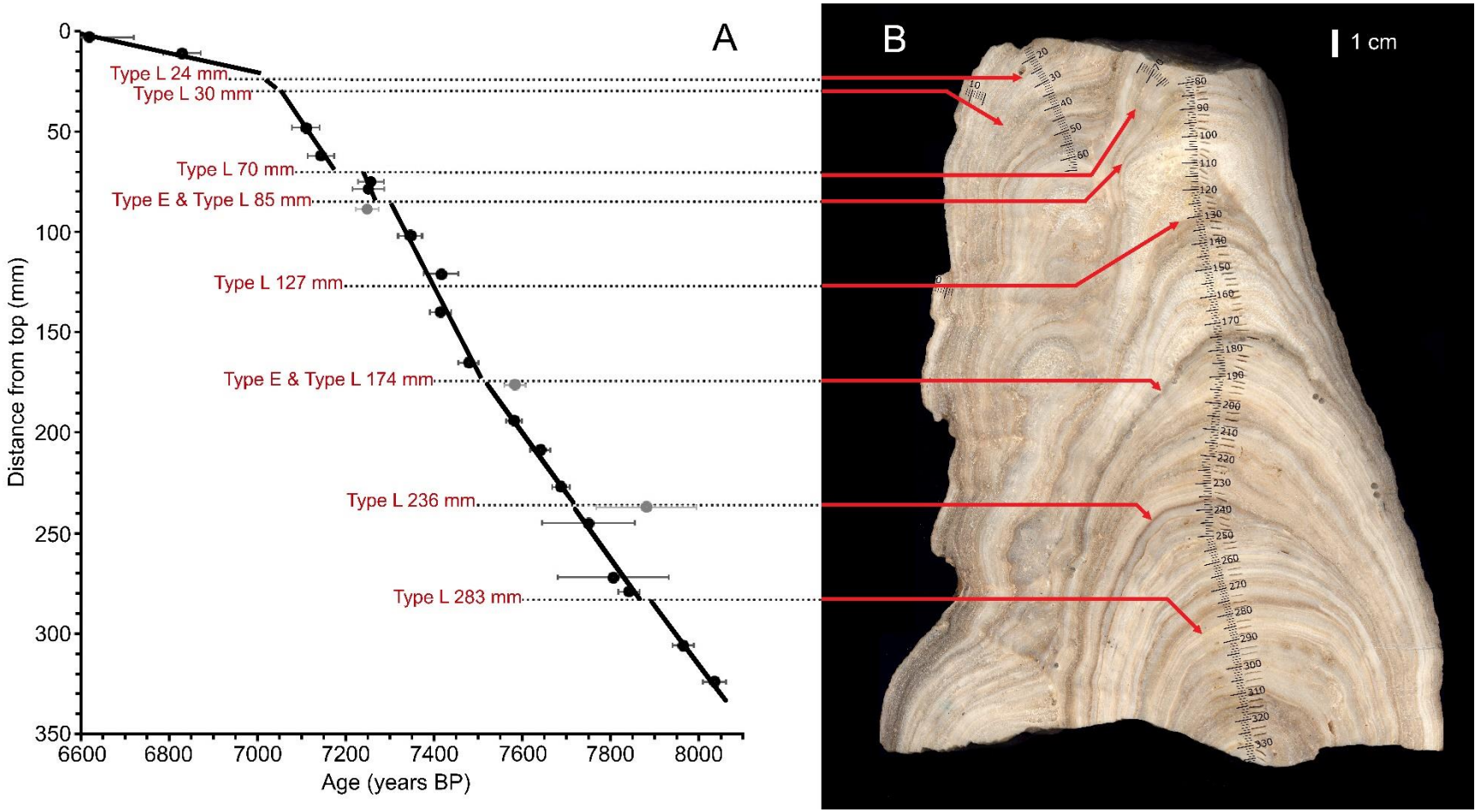
A
B
1 cm
Type L 24 mm
Type L 30 mm
Type L 70 mm
Type E & Type L 85 mm
Type L 127 mm
Type E & Type L 174 mm
Type L 236 mm
Type L 283 mm
Distance from top (mm)
Age (years BP)
0
50
100
150
200
250
300
350
6600
6800
7000
7200
7400
7600
7800
8000

Figure 10. Selected X-ray diffraction plots. The uppermost plot, MAT12-XRD1, shows a sample that is 100% aragonite. The middle plot, MAT-12-XRD9, shows an intermediate sample that is 46% aragonite. The lower plot, MAT12-XRD7, shows a sample that is 0% aragonite (i.e., 100% calcite).

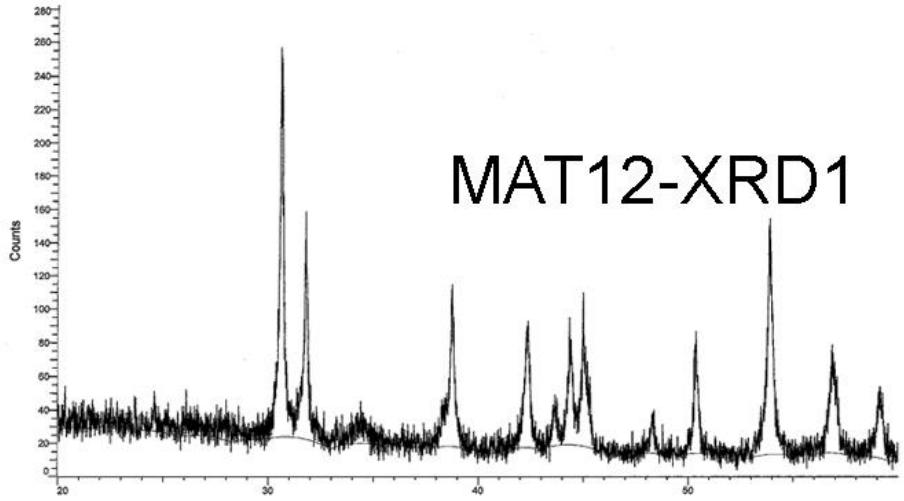
MAT12-XRD1
Counts

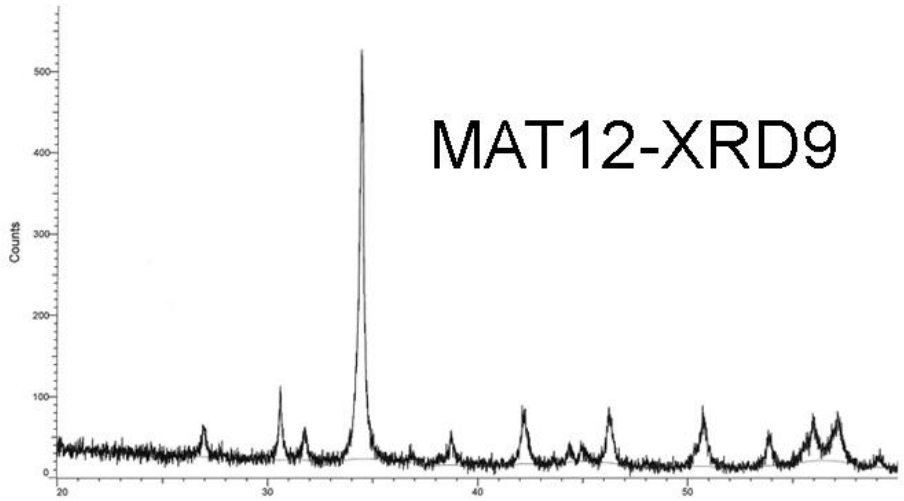
MAT12-XRD9
Counts

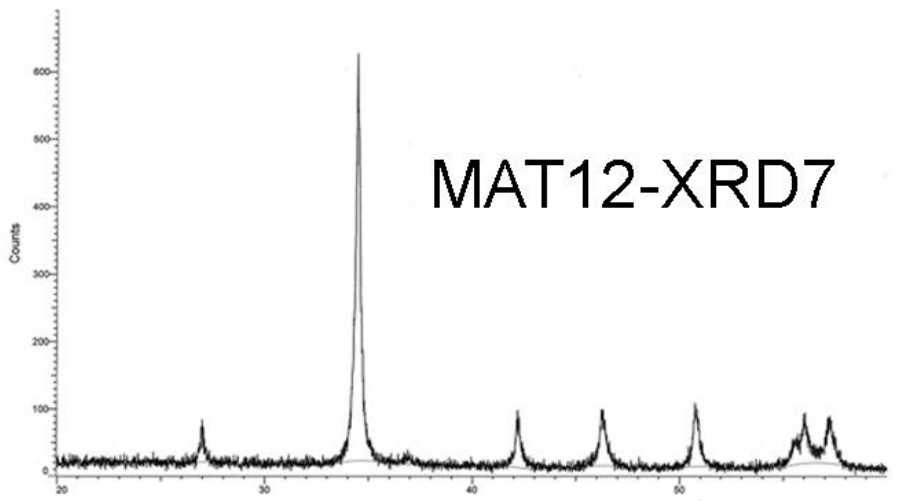
MAT12-XRD7
Counts

CHAPTER 5: DISCUSSION

5.1. Stalagmite MAT-12 proxies as paleoenvironmental indicators

Of the various ways that proxy measurements from stalagmites can be applied to paleoenvironmental reconstruction, this study has opted for the simplest applications to ensure the results are constrained within the region local to Matupi Cave and to avoid exaggerated conclusions. Here, the principles guiding interpretation of the petrographic and isotopic proxies from Stalagmite MAT-12 are defended and unique applications are explained as those four proxies are used to reconstruct the environment of central equatorial Africa near Matupi Cave during the African Humid Period (Table 2, Fig. 11).

5.1.1. Layer-bounding surfaces

Type E layer-bounding surfaces are evidence of erosion caused by wetter conditions within the cave, and Type L layer-bounding surfaces are evidence of lessened deposition caused by drier conditions within the cave (Section 3.3., Railsback et al., 2013). Changes in the amount of water entering the cave as dripwater are controlled by shifts in regional rainfall and by changing features in the epikarst, suggesting that layer-bounding surfaces can be applied as evidence of changing hydroclimate. The presence of layer-bounding surfaces also indicates the presence of hiatuses as Type E surfaces require non-representation of the time of dissolution and of the time in which dissolved layers were deposited (Railsback et al., 2013). Similarly, Type L surfaces suggest, but not necessarily require, that some time is not represented after the most diminished layers.

All the above is true for Stalagmite MAT-12, with an additional suggestion offered by the distinct case of the two Type E surfaces that overlie Type L surfaces. These surfaces may indicate that conditions within the cave gradually dried, and, at some later time, conditions were wet enough to erode those layers that indicate lessened deposition. These surfaces, however, raise more questions than they answer: The environmental conditions are still unknown because any amount of the Type L surface, and therefore the record of drier conditions, could have been eroded by the wetter conditions suggested by the overlying Type E surface. The transition between dry and wet conditions may have been rapid, or the transition between dry and wet could have been separated by intermediate conditions that precipitated normal stalagmite layers that were later eroded. The latter suggestion could explain the longest hiatus of the record of Stalagmite MAT-12 of 90 years between 7160 yr BP and 7250 yr BP (Fig. 11). The remaining six Type L surfaces not associated with Type E surfaces simply represent periods of decreased rainfall and short hiatuses that have been accounted for in the construction of the age model (Fig. 9).

5.1.2. Growth rate

The application of growth rate data to stalagmite reconstructions poses various challenges. The prevalent application in stalagmite reconstructions argues that growth rate is always positively and monotonically related to atmospheric precipitation rate (i.e., increased rainfall always produces faster growth rates) (e.g., Dreybrodt and Franke 1987; Kaufmann, 2003; Kaufmann and Dreybrodt, 2004; Mühlinghaus et al., 2007; Dreybrodt, 2016). From a compilation of data from modern stalagmites, Railsback (2018) concluded that the relationship between growth rate, atmospheric precipitation, and temperature is

more complex because this relationship is highly dependent on the wetness of climate and the inter-annual relationship between temperature and rainfall of the reconstruction setting (Railsback 2018, Fig. 14). This suggests that growth rate is only a useful proxy in environments where both temperature and precipitation mutually control growth rate to cause a monotonic-positive relationship to growth rate or a monotonic-negative relationship to growth rate. In some cases, temperature change and precipitation have counteracting effects on growth rate, negating the use of growth rate data in those settings (Railsback 2018, Fig. 14). Likewise, in more temperate settings, growth rate of stalagmites is non-monotonic, making it a poor proxy for precipitation and confounding its application as a proxy for temperature (Railsback 2018, Fig. 14).

The growth rate of Stalagmite MAT-12 is interpreted as an inverse relationship between growth rate and rainfall: decreased growth rate represents increased rainfall. When considering the relationship between growth rate and rainfall at Matupi Cave, modern average annual atmospheric precipitation (approximately 1200 mm/yr) and an estimate of average annual atmospheric precipitation at ca. 8000 yr BP (approximately 1600–1800 mm/yr) were applied to Figure 4 in Railsback (2018) (Fig. 12). In both cases, these precipitation rates suggest that growth rate has an inverse relationship with increasing precipitation, as suggested by results from stalagmites in similar environments where both growth rate and annual atmospheric precipitation rate were known. For this reason, the growth rate results from Stalagmite MAT-12 are interpreted as slower growth rates represent wetter conditions, and faster growth rates represent drier conditions.

Those growth rate results suggest that the intermediate growth rate early in the record (ca. 8050), followed by the dramatic drop after a hiatus at 7841 yr BP, and the

similarly slow growth rate after the hiatus at 7695 yr BP represent a pronounced wet period at the beginning of the record (Fig. 11a). After the hiatus at 7472 yr BP, growth rate dramatically increases, suggesting a rapid transition to dry conditions.

5.1.3. Mineralogy

Here, pure aragonite samples are assumed to represent drier conditions and pure calcite samples are assumed to represent wetter conditions (Railsback et al. (1994) and sources cited therein). The first sample of 100 % aragonite suggests that Matupi Cave was relatively dry shortly after deposition began at ca. 8000 yr BP. Three samples of 0 % aragonite (or 100 % calcite) suggest a pronounced wet period from 7819–7952 yr BP (Fig. 11b). This pronounced wet period is followed by a period of fluctuation between pure calcite and intermediate samples, potentially suggesting gradual dryness until after the hiatus at 7493 yr BP when continuously pure aragonite samples suggest continuously dry conditions (Fig. 11b).

5.1.4. Layer-specific width measurements

Layer-specific width suggests a timeline that matches well with both the growth rate data and the mineralogical data (Fig. 11c). Layer-specific width is interpreted as smaller layer-specific width values represent drier conditions, and greater layer-specific width values represent wetter conditions (Sletten et al., 2013; Railsback et al., 2014). Layer-specific width measurements indicate that conditions at Matupi Cave were relatively dry at 7972 yr BP. A pronounced wet period follows this dry start from 7663–7918 yr BP.

The record then gradually trends towards drying until 7429 yr BP when the record suggest conditions were continuously dry until 7274 yr BP.

5.1.5. Oxygen stable isotopes

In this study, $\delta^{18}O$ is interpreted as a proxy for amount of atmospheric precipitation, where smaller values indicate wetter conditions because of an amount effect (e.g., McDermott, 2004; Lachniet, 2009; Table 2 and citations therein). This suggests that the $\delta^{18}O$ record of Stalagmite MAT-12 indicates gradual drying from the beginning of the record at 8034 yr BP to the end of the record at 6790 yr BP, with a few wet excursions at 7687 yr BP, 7639 yr BP, 7578 yr BP, and 7544 yr BP (Fig. 11d). All four of these wet excursions occur before the hiatus at 7532 yr BP and suggest brief periods of increased rainfall.

5.1.6. Carbon stable isotopes

The $\delta^{13}C$ results are interpreted as a proxy for both vegetation extent, where smaller $\delta^{13}C$ represents more vegetation cover, and as a proxy for photosynthetic pathway of that vegetation, where smaller $\delta^{13}C$ values represent C_3 plants and larger $\delta^{13}C$ values represent C_4 plants (Rieley et al., 1993; Collister et al., 1994; Table 2 and citations therein). This implies that $\delta^{13}C$ results can be connected to changing hydroclimate as expanded vegetation cover can be linked to periods of increased wetness that would support the plant communities present near Matupi Cave. Transitions between dominant photosynthetic pathways in equatorial Africa are also relevant as shifts between wet Moraceae C_3 trees

and hot, wet C_4 Poaceae grasses are linked to changing hydroclimate (e.g., Kendall 1969; Berke et al., 2012; Berke et al., 2014).

The $\delta^{13}C$ results from Stalagmite MAT-12 suggest four wet excursions at the pronounced low points at 7687 yr BP, 7639 yr BP, 7578 yr BP, and 7544 yr BP before the hiatus at 7532 yr BP (Fig. 11e). During these four wet excursions, dense C_3 tropical trees would have been present in the environment overlying Matupi Cave. Increasing $\delta^{13}C$ values after at least ca. 7400 yr BP indicate a gradual shift towards drying, where vegetation overlying the cave may have slowly transitioned to C_4 hot grasses.

5.2. Stalagmite MAT-12 paleoenvironmental reconstruction: Three theories

The petrographic results and the stable isotope results from Stalagmite MAT-12 suggest two different paleoenvironmental reconstructions of changing conditions near Matupi Cave. A third theory suggests that the finer details of those reconstructions (both petrographic and isotopic) are insignificant and that the reconstruction this study provides must be viewed within the greater temporal and spatial scope of African Humid Period reconstructions in equatorial Africa.

5.2.1. Petrographic record of intermediate-wet-intermediate conditions

Three of the petrographic proxies sampled from Stalagmite MAT-12 suggest that conditions at Matupi Cave were intermediate at the beginning of the record, followed by a pronounced wet period and a subsequent return to intermediate conditions. Though the growth rate data set and the percent aragonite data sets differ in how quickly the environment transitions to intermediate conditions, the three data sets loosely agree on

when that environmental shift occurred. Additionally, the layer-specific width data set can be viewed as an intermediary between the growth rate data set and the percent aragonite data set. The timing of the pronounced wet period suggested by the layer-specific width data is most like the timing of the pronounced wet period suggested by the growth rate data that indicates intermediate dryness at ca. 8050 yr BP followed by a somewhat later pronounced wet period from ca. 7650–7900 yr BP. The layer-specific width results then more closely align with the mineralogy results, indicating a gradual transition from wet to dry until ca. 7400 yr BP where the smallest measurements suggest dry conditions.

This implies the petrographic proxy results from Stalagmite MAT-12 can be loosely summarized to suggest that conditions near Matupi Cave during the African Humid Period were drier from ca. 7900–8050 yr BP, followed by a pronounced wet period from ca. 7700–7900 yr BP. Intermediate conditions characteristic of a gradual hydroclimate transition are potentially present from ca. 7500–7700 yr BP. Thereafter, conditions near Matupi Cave were dry until the stalagmite ceased deposition, ca. 6800–7500 yr BP.

When considering the modern environments of AHP sites, Matupi Cave is much wetter than other equatorial Africa AHP sites (Section 2.3., Fig. 4). This is particularly distinct in the Köppen-Geiger classifications (Beck et al. 2018) of the sites, where Matupi Cave and all central equatorial Africa are some variation of “tropical” classifications. Though some tropical classifications are also present in southeastern equatorial Africa, the AHP sites from southeastern equatorial Africa and northeastern equatorial Africa are classified as “temperate” or “arid”. This suggests that drier periods at Matupi Cave were likely remarkably more wet than the dry conditions of nearby AHP sites and highlights the challenge of AHP studies that utilize comparative terms. This leads to the suggestion that

this reconstruction from a tropical region in central equatorial Africa should be considered as a record of intermediate conditions from ca. 7900–8050 yr BP, wet conditions from ca. 7700–7900 yr BP, and intermediate conditions from ca. 6800–7700 yr BP when compared to drier eastern equatorial Africa AHP sites characterized by the relative terms wet, intermediate, and dry. The distinction between the previously suggested periods of intermediate conditions ca. 7500–7700 yr BP and dry conditions ca. 6800–7500 yr BP is lost as these dry conditions are presumably too wet to match the use of the word dry in other publications.

5.2.2. Isotopic record of gradual wet to intermediate transition

The $\delta^{13}C$ and the $\delta^{18}O$ records from Stalagmite MAT-12 both suggest a gradual transition from wet conditions to intermediate conditions throughout the record from ca. 6800–8050 yr BP.

Both the $\delta^{13}C$ and the $\delta^{18}O$ records identify four wet excursions near the beginning of the record at 7687 yr BP, 7639 yr BP, 7578 yr BP, and 7544 yr BP before the hiatus at 7532 yr BP (Fig. 11d and e). Two pronounced low points at the beginning of the $\delta^{13}C$ record at 8012 yr BP and 7792 yr BP do not correlate with the $\delta^{18}O$ data, suggesting that no definitive conclusions can be drawn from these excursions. Later in the $\delta^{13}C$ record, a few pronounced highs may appear to imply dry excursions after the hiatus at 7532 yr BP, but these data points again do not correlate well with the $\delta^{18}O$ data. At most, the two data sets work together to suggest gradual drying in the environment overlying Matupi Cave as Stalagmite MAT-12 deposited from ca. 6800–8050 yr BP, with a few brief moments of increased rainfall between ca. 7500 yr BP and ca. 7700 yr BP.

5.2.3. Matupi Cave as a record of wet conditions

The nuance of the relative terms wet, intermediate, and dry continue to require close attention when attempting to compare the results from Matupi Cave to other equatorial Africa AHP sites (Section 5.2.1.). With this in mind, the reconstruction provided by Stalagmite MAT-12 could be viewed simply as a record of wet conditions at Matupi Cave during its deposition from ca. 6800–8050 yr BP in the middle of the African Humid Period. In the most fundamental sense, the deposition of a stalagmite indicates that conditions at the site were at least wet enough to supply water to travel through the epikarst and to support vegetation communities vital to the reaction that causes $CaCO_3$ precipitation. This suggests that the entire record of Stalagmite MAT-12 from ca. 6800–8050 yr BP reconstructs wet conditions at Matupi Cave.

This suggestion from Stalagmite MAT-12 is strengthened by two other Matupi Cave stalagmites currently under study. Stalagmite MAT-23 and Stalagmite MAT-1, collected from Matupi Cave during the same field season as Stalagmite MAT-12, have already been sampled for radiometric ages. Stalagmite MAT-23 was deposited from ca. 15,500–16,400 yr BP and may reconstruct the environmental conditions at Matupi Cave prior to the onset of the AHP at ca. 14,800 yr BP. Stalagmite MAT-1 was deposited from ca. 3100–5200 yr BP and may reconstruct the environmental conditions at Matupi Cave following the termination of the AHP at ca. 5500 yr BP. As with Stalagmite MAT-12, the precipitation of these additional stalagmites indicates that conditions at Matupi Cave were at least wet enough to support stalagmite deposition. The three Matupi Cave stalagmites can be viewed as records of wet conditions while those stalagmites were deposited in the late Pleistocene to the mid-Holocene.

5.3. Contribution to AHP records

The paleoenvironmental record of Stalagmite MAT-12 makes notable contributions to the current understanding of the geographic extent, timing, and causes of the African Humid Period in central equatorial Africa.

5.3.1. Geographic extent: The African Humid Period is apparent at Matupi Cave

In the most basic interpretation, the reconstruction from Stalagmite MAT-12 suggests that the African Humid Period occurred at Matupi Cave. While this is a simple statement, it is a useful addition to AHP records from equatorial Africa. The location of Matupi Cave suggests that the record of Stalagmite MAT-12 serves as a more western record of the AHP in equatorial Africa and so extends the geographic range of equatorial AHP sites (Fig. 13). Likewise, Matupi Cave is a unique site because of its location within the western branch of the East African Rift as other equatorial AHP sites are primarily within the eastern branch.

This reconstruction also suggests that the AHP is apparent in wetter regions of equatorial Africa. As most other equatorial AHP sites are from drier regions in eastern equatorial Africa, the reconstruction from Stalagmite MAT-12 serves as one of the first AHP records from a tropical site in central equatorial Africa.

5.3.2. Timing: Stalagmite MAT-12 can attest to the intensity of the middle of the African Humid Period

The results from Stalagmite MAT-12 reconstruct a brief period of time within the African Humid Period and provide a few insights into the question of timing of the AHP

in equatorial Africa. When compared to other AHP records from equatorial Africa, Stalagmite MAT-12 was deposited during the height of the AHP recognized at most sites (Fig. 14, Table 3). This strengthens the idea that Stalagmite MAT-12 is a record of wet conditions during the AHP from ca. 6800–8050 yr BP (Section 5.3.3.), but does not necessarily negate the more detailed reconstructions suggested by the petrographic (Section 5.3.1.) and the isotopic data (Section 5.3.2.).

The two proxy reconstructions from Stalagmite MAT-12 of the petrographic and isotopic data both indicate a shift from wet conditions to intermediate conditions at Matupi Cave at ca. 7700 yr BP. This may suggest that the transition out of the AHP was gradual rather than rapid. Many of the selected reconstructions from AHP sites in equatorial Africa suggest that following intense wetness in the early Holocene, environmental conditions gradually shifted to become drier (Fig. 14, Table 3). Only two sites, Lake Turkana in northeastern equatorial Africa and Mt. Kilimanjaro in southeastern equatorial Africa, suggest environmental conditions rapidly shifted from wet to dry in the mid-Holocene (Sites 5 and 9, Fig. 14, Table 3).

The deposition of Stalagmite MAT-12 within such a brief period at the peak of the AHP may further suggest that the AHP can only be identified at tropical sites during the most intense wet periods. Considering the position of Matupi Cave on the western margin of the Congo River Basin, this may imply that sites deeper into central equatorial Africa that can identify the AHP are unlikely due to the intense wet conditions that persist in the region year-round.

The brief reconstruction that Stalagmite MAT-12 provides from ca. 6600–8050 yr BP clearly cannot provide a reconstruction for the entire AHP, ca. 5500–14,800 yr BP. To

strengthen the applicability of this reconstruction to future AHP studies, the results from Stalagmite MAT-23 (deposited ca. 15,500–16,400 yr BP) and Stalagmite MAT-1 (deposited ca. 3100–5200 yr BP) will be included in the manuscript that develops from this document. The culmination of the results from these three stalagmites will form a reconstruction that can attest to the environmental conditions at Matupi Cave before, during the height of, and after the AHP, and so will provide a more robust reconstruction of the AHP.

5.3.3. Cause: Stalagmite MAT-12 confirms the insolation-driven nature of the African Humid Period

The deposition of Stalagmite MAT-12 and the other two Matupi stalagmites confirms the well-established concept that the African Humid Period was caused by increased solar insolation in the north African subtropics. Modern Matupi Cave experiences greatest insolation during the equinoxes in March and September which causes migration of the tropical rain belt and the onset of the rainy seasons in March–May and September–November (Section 2.3.). This modern connection between insolation and rainfall at Matupi suggests that seasonal variation in insolation may be significant over time. When insolation during the months of the equinox (March and September) and the months immediately before and after each of those equinoxes (February/April and August/October) are plotted throughout the AHP, a relationship between the deposition of the Matupi stalagmites and of periods of maximum insolation is apparent: All three stalagmites were deposited during insolation peaks (Fig. 15). The two insolation maxima at the March equinox at ca. 16,000 yr BP and at the September equinox at ca. 6000 yr BP

would have caused increased rainfall at those times to support the deposition of the Matupi stalagmites.

This suggests that Stalagmite MAT-23 was deposited during a period before the AHP that experienced a dramatic rainy season during the March equinox (February–April). Stalagmite MAT-12 and Stalagmite MAT-1 were later deposited when a dramatic rainy season occurred during the September equinox (August–October), where Stalagmite MAT-12 deposited prior to the insolation maxima and Stalagmite MAT-1 deposited following the insolation maxima.

The link between changing hydroclimate and stalagmite deposition necessarily involves infiltration through the epikarst into the cave. If one considers the argument that stalagmites are, more directly, records of infiltration rather than regional hydroclimate, the deposition of stalagmites would be correlated to strong rainy seasons. This could explain the deposition of the Matupi stalagmites that deposited during periods of one very strong rainy season followed by a weak rainy season. The strong rainy season would cause increased infiltration to move more water through the epikarst into the cave. Likewise, the link between infiltration and stalagmite deposition could explain why this record lacks stalagmites around ca. 11,000 yr BP because the two rainy seasons at Matupi Cave would have had similar strength. In other words, solar insolation caused seasonality at Matupi Cave to be too weak to increase infiltration to promote stalagmite deposition.

Furthermore, this relationship between insolation and rainfall supports the theory that the distinction between the shifts of wet and intermediate conditions in the record of Stalagmite MAT-12 are inconsequential and that Stalagmite MAT-12 is simply a record of wet conditions during the AHP. The strong rainy season from August–October strengthens

throughout the deposition of Stalagmite MAT-12, implying that conditions at Matupi were increasingly, or at least continuously, wet. This opposes the petrographic and isotopic reconstructions that both identify gradual drying at the end of the record. Optimistically, the results from Stalagmite MAT-1 can improve the interpretation of the data from Stalagmite MAT-12 to confirm whether Stalagmite MAT-12 is recording a gradual transition toward drying at the end of the AHP or whether the trend towards drier conditions should still be considered wet when compared to other AHP records.

5.4. Limitations

As with any paleoenvironmental reconstruction, the results from Stalagmite MAT-12 are limited. In terms of geographic limitations, stalagmite data can often only be applied in a regional context. This reconstruction from Matupi Cave can only attest to conditions in central equatorial Africa. This idea continues to become more apparent in other African Humid Period literature utilizing different proxies as distinctions between site conditions in different regions of Africa are recognized (e.g., Costa et al., 2014; Shanahan et al., 2015). Though this study provides a new, high-resolution record of the AHP, Stalagmite MAT-12 does not record the bulk of the AHP, including its onset and termination. This limits this study's ability to comment on those issues that are still widely debated. The addition of the reconstructions from Stalagmite MAT-23 and Stalagmite MAT-1 will strengthen the validity of the Stalagmite MAT-12 data set when considering the AHP in its entirety. Additionally, the Stalagmite MAT-12 reconstruction cannot be used to make statements about land-surface feedbacks and moisture sourcing like other paleoclimate proxies that record the AHP (e.g., δD_{wax} in Tierney et al., 2011b and major elemental ratios in Liu et al., 2017).

Table 2. Controls and climate significance of stalagmite proxies. An asterisk (*) indicates the immediate controls for $\delta^{18}O$ and $\delta^{13}C$ for Stalagmite MAT-12. Adapted from Table 1 of Voarintsoa et al. (2017).

Proxies	Definition/controlling factors	References
$\delta^{18}O$	$\delta^{18}O = [(^{18}O/^{16}O)_{sample} - (^{18}O/^{16}O)_{standard})]/(^{18}O/^{16}O)_{standard}$ • Variations in $\delta^{18}O$ of moisture source supplying drip water to the cave. This is mainly significant to decipher glacial (greater $\delta^{18}O$) and interglacial intervals (smaller $\delta^{18}O$). • Variations in atmospheric temperature: although $\delta^{18}O$ values are typically lower in the winter and higher in the summer in several regions, the opposite has been observed in Madagascar (greater $\delta^{18}O$ during winter, smaller $\delta^{18}O$ during summers, Figs. 2 and S4) • Distance of transport from the vapor source (continental effect): typically water $\delta^{18}O$ values decrease with distance from the ocean, but it could be influenced by high $\delta^{18}O$ recycled continental moisture back to the atmosphere from evaporation of soil water, lakes, and rivers. • Altitude effect: smaller $\delta^{18}O$ with increasing elevation. • * variations in the $\delta^{18}O_w$ of the dripwater which reflect the $\delta^{18}O$ of atmospheric precipitation (amount effect). It varies depending on seasonality of rainfall (e.g. in tropical warm summers, $\delta^{18}O$ is smaller with increased rainfall amount; whereas in mid-latitude colder regions, mean winter rainfall is often more depleted in ^{18}O) • Variations in cave temperature: greater $\delta^{18}O$ with colder temperature, and smaller $\delta^{18}O$ with warmer temperature • Magnitude of kinetic fractionation of dripwater or water films precipitating carbonate • Evaporation inside and outside the cave: greater $\delta^{18}O$ with increased evaporation.	Burns et al., 2002 Clark and Fritz, 1997 Cuthbert et al., 2014 Dansgaard, 1964 Deininger et al., 2012 Fairchild and Treble, 2009 Hoefs, 2009 Koster et al., 1993 Lachniet, 2009; McDermott, 2004 Quade, 2004 Railsback, 2010 Rozanski et al., 1993 Wong and Breecker, 2015

$\delta^{13}C$	$\delta^{13}C = [(^{13}C/^{12}C)_{sample} - (^{13}C/^{12}C)_{standard})]/(^{13}C/^{12}C)_{standard}$
	• Variations of $\delta^{13}C$ of CO_2 in the atmosphere
	  • Smaller $\delta^{13}C$ due to the Suess effect
	  • Smaller $\delta^{13}C$ during glacial and greater $\delta^{13}C$ during interglacial
	• * photosynthetic pathway: smaller $\delta^{13}C$ for C_3 plants and greater $\delta^{13}C$ for C_4 plants.
	• * extent of vegetation, soil biomass productivity (as a function of meteoric precipitation): smaller $\delta^{13}C$ with more vegetation cover
	• rate of passage of water through soil to limestone
	  • Closed system: greater $\delta^{13}C$ with faster passage if water and thus lesser input of soil CO_2
	  • Open system: lesser $\delta^{13}C$ with slower passage of water and thus greater input of soil CO_2
	• $\delta^{13}C$ of limestone
	• extent of degassing of CO_2 and Prior Calcite Precipitation (or more generally Prior Carbonate Precipitation). The relationship between degassing and prior calcite precipitation results in systematic rises in $\delta^{13}C$.
	• Cave ventilation which could accelerate the rate of degassing and PCP, leading to an increase in $\delta^{13}C$.
		Baldini et al., 2005
		Brook et al., 1999, 2010
		Brook et al., 2006
		Burns et al., 2016
		Cross et al., 2015
		Cruz et al., 2006
		Denniston et al., 2013
		Dreybrodt and Scholz, 2011
		Fairchild and McMillan, 2007
		Frisia et al., 2011
		Genty et al., 2001, 2003, 2006
		Hesterberg and Siegenthaler, 1991
		Johnson et al., 2006
		Lauritzen and Lundberg, 1999
		Meyer et al., 2014
		Mickler et al., 2004, 2006;
		Moreno et al., 2010

Proxies	Definition/controlling factors	References
Layer bounding surfaces	Surfaces between two spelean layers that delimit series of layers and represent periods of non-deposition Type E: surfaces below which spelean layers are truncated, microscopic examination shows signs of dissolution • Type E surfaces represent exceptionally wet conditions and faster drip rate. Type L: surfaces below which layers thin upward and/or have lesser lateral extent upward (the layer-specific width decreases) • Type L surfaces represent exceptionally dry conditions and slower drip rate.	Quade, 2004 Railsback, 2010 Suess, 1955 Verburg, 2007 Wong and Breecker, 2015 Railsback et al., 2011, 2013 Sletten et al., 2013 Voarintsoa et al., 2016
Layer-specific width	The width across the stalagmite between the points at which the layer is tangent to a line inclined at specific angle (here it is 10°) relative to the growth axis of the stalagmite • Smaller values represent drier conditions and reduced drip rate. • Greater values represent wetter conditions and increased drip rate.	Dreybrodt (1999) Railsback et al., 2014 Sletten et al., 2013 Yadava et al., 2004
Mineralogy	There are several spelean minerals but the most common ones are calcite and aragonite. Factors directly favoring the formation of aragonite, rather than calcite, under cave conditions are: • high temperature, • drip water composition in trace elements (high concentration of Mg, Sr, Pb), which could reflect the composition of the bedrock • drier conditions • extensive evaporation • seasonal dryness • prior carbonate precipitation	Bischoff and Fyfe, 1968 Bischoff, 1968 Cabrol and Coudray, 1982 Caddeo et al., 2011 Fischbeck, 1976 Frisia et al., 2002 González and Lohmann, 1988 Hill and Forti, 1997 McMillan et al., 2005 Moore, 1956 Murray, 1954 Pobeguin, 1965 Railsback et al., 1994; Railsback, 2000 Riechelmann et al., 2014 Siegel, 1965 Sletten et al., 2013 Thrailkill, 1971

Table 3. Equatorial Africa site information. Data from AHP studies near Matupi Cave, equatorial Africa. Sites are numbered in ascending order of distance from Matupi Cave, where the closest site is Lake Edward, site 2, and the farthest site is Lake Challa, site 10. Adapted from Supplementary Table A of Liu et al., (2017).

No.	Name	Lat.	Long.	Proxies	Humid period	Termination	Drought	References
8	Chew Bahir	4.83	36.77	K	11.6-6 ka	6-5 ka gradual	8.8-7.5 ka	Foerster et al. (2012)
5	Lake Turkana	3.43	36.06	Shoreline	11.5-5.3 ka	5.3 ka abrupt	8.5 ka	Garcin et al. (2012)
6	Lake Suguta	2.00	36.50	Shoreline	11.5-6.7 ka	6.7-5 ka gradual	8.3 ka	Junginger et al. (2014)
1	Matupi Cave	1.19	30.01	Multi	8.0-6.8 ka			This study, Dupont 2021
3	Pilkington Bay	0.08	32.80	Diatom	~9.5-5.8 ka	gradual	8.3-7.8 ka	Stager et al. (2003)
2	Lake Edward	-0.32	29.58	Calcite	11-5.2 ka	5.2-4 ka gradual		Russell et al. (2003)
7	Lake Naivasha	-0.78	36.35	Pollen	14.3-7.4 ka	7.4-4.5 ka gradual		Maitima (1991)
4	Lake Victoria	-1.23	33.20	$\delta D_{leaf\ wax}$	10-4.7 ka	8-4.7 gradual		Berke et al. (2012)
9	Mt Kilimanjaro	-3.08	37.35	$\delta^{18}O$	11-4 ka	gradual	8.4 ka	Thompson et al. (2002)
10-1	Lake Challa	-3.32	37.70	BIT index	14.5-8.5 ka	gradual		Verschuren et al. (2009)
10-2	Lake Challa	-3.32	37.70	$\delta D_{leaf\ wax}$	10-5 ka	5 ka abrupt		Tierney et al. (2011)
10-3	Lake Challa	-3.32	37.70	$\delta^{18}O_{diatom}$	14.5-8 ka	8-4 ka gradual		Barker et al. (2011)

Figure 11. Stalagmite MAT-12 results vs. time (years BP), where BP stands for "Before Present" and "present" is the year 1950 AD. Each plot is oriented so that drier conditions are up and wetter conditions are down. Hiatuses are marked with vertical gray bars as indicated by petrographic surfaces that have been incorporated into the age model. (A) Growth rate data from the main axis in mm per year. (B) X-ray diffraction/mineralogy data expressed as percent aragonite, where 0 % is entirely calcite. (C) Layer-specific width measurements from the main axis in mm as measured by two separate analysts (1. L.B. Railsback and 2. L.A. Dupont). (D) $\delta^{18}O$ data from the entirety of Stalagmite MAT-12, including the left flank, vs. VDPB. Several low points correlate with data from (E) $\delta^{13}C$ data from the entirety of Stalagmite MAT-12, including the left flank, vs. VDPB.

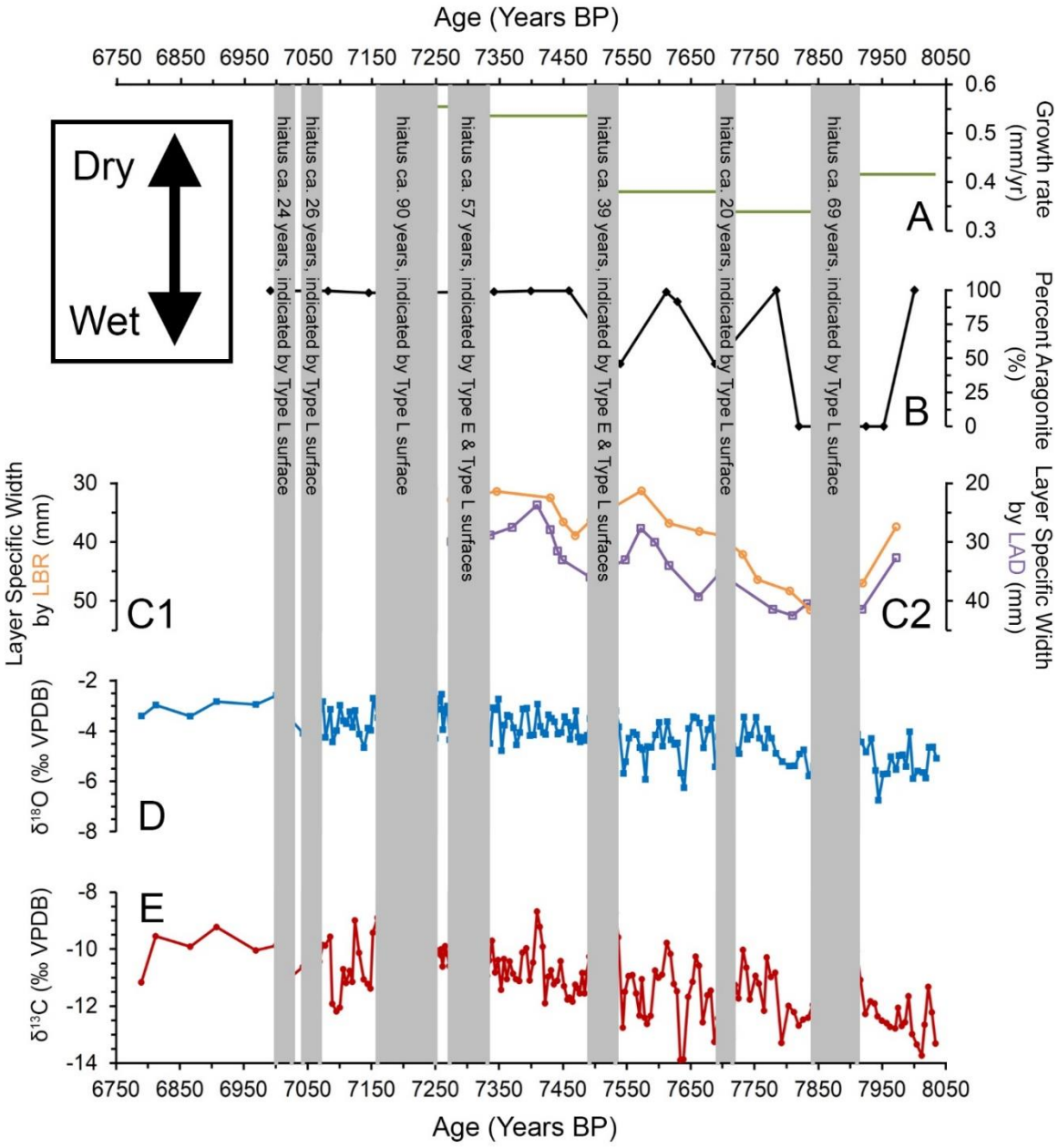
Age (Years BP)
6750 6850 6950 7050 7150 7250 7350 7450 7550 7650 7750 7850 7950 8050
Dry
Wet
hiatus ca. 24 years, indicated by Type L surface
hiatus ca. 26 years, indicated by Type L surface
hiatus ca. 90 years, indicated by Type L surface
hiatus ca. 57 years, indicated by Type E & Type L surfaces
hiatus ca. 39 years, indicated by Type E & Type L surfaces
hiatus ca. 20 years, indicated by Type L surface
hiatus ca. 69 years, indicated by Type L surface
Growth rate (mm/yr)
0.6
0.5
0.4
0.3
A
Percent Aragonite (%)
100
75
50
25
0
B
Layer Specific Width by LBR (mm)
30
40
50
C1
Layer Specific Width by LAD (mm)
20
30
40
C2
δ18O (‰ VPDB)
-2
-4
-6
-8
D
δ13C (‰ VPDB)
-8
-10
-12
-14
E
6750 6850 6950 7050 7150 7250 7350 7450 7550 7650 7750 7850 7950 8050
Age (Years BP)

Figure 12. Principle guiding growth rate interpretation. Adapted Figure 4 from Railsback (2018), a plot of growth rates of 81 stalagmites during the Holocene relative to the average annual atmospheric precipitation in the environment overlying the cave. The filled circles indicate stalagmite growth in the later Holocene, mostly in the recent 3000 years, and one open circle indicates stalagmite growth from the earlier Holocene that was selected because it is from a region with exceptional rainfall (Dutt et al., 2015). Five green curves indicate result from stalagmites in which growth rate was correlated with known variation in annual atmospheric precipitation (Cai et al., 2010; Kato and Yamada, 2016; Proctor et al., 2000; Railsback et al., 1994; Rasmussen et al., 2006). The figure has been adapted to show present atmospheric precipitation near Matupi Cave (1350 mm) and past atmospheric precipitation, ca. 8000 yr BP, near Matupi Cave (approx. 1600-1800 mm). Both plotted rainfalls suggest that the relationship between growth rate and rainfall near Matupi Cave is most like three nearby green curves that suggest an inverse relationship between growth rate and annual precipitation, (i.e., slower growth rates indicate wetter conditions, and faster growth rates indicate drier conditions).

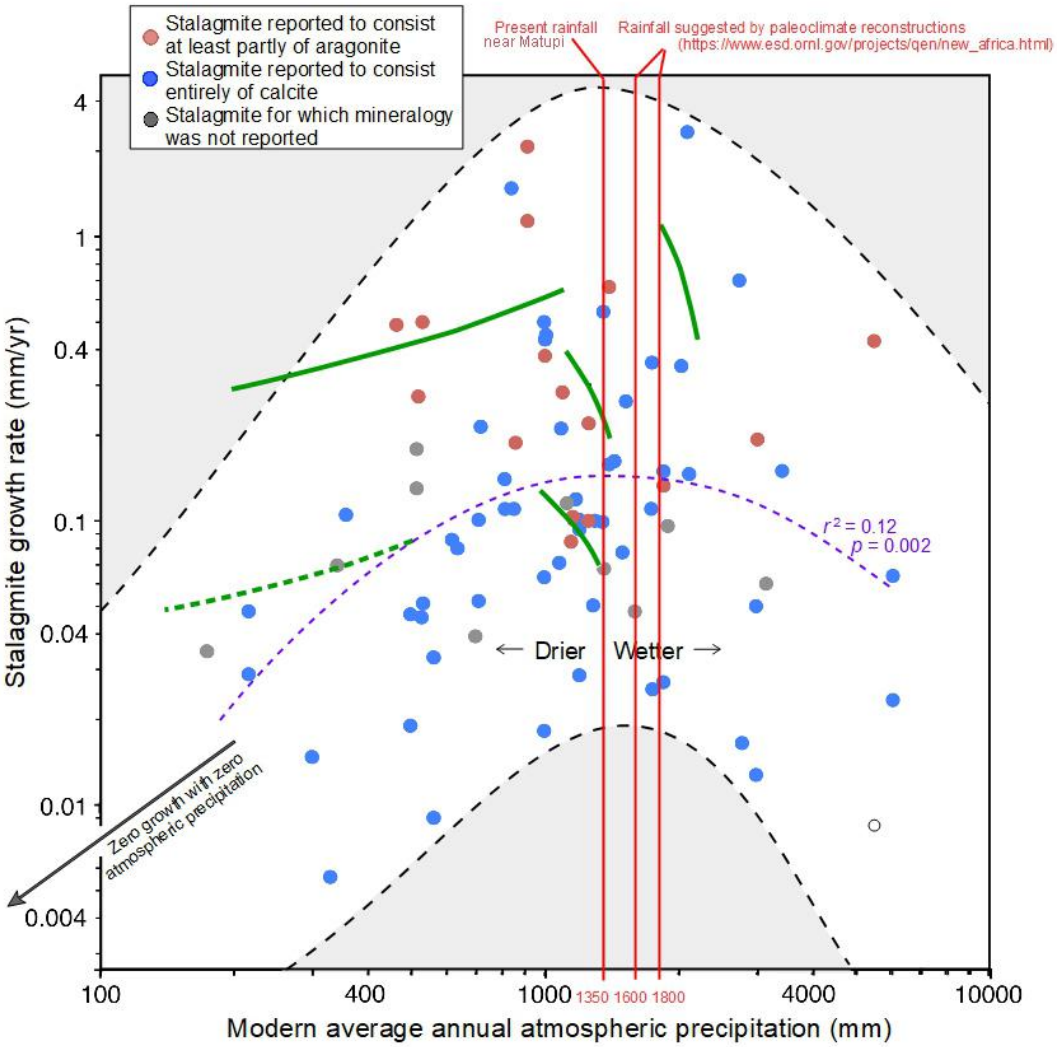
Stalagmite reported to consist at least partly of aragonite
Stalagmite reported to consist entirely of calcite
Stalagmite for which mineralogy was not reported
Present rainfall near Matupi
Rainfall suggested by paleoclimate reconstructions (https://www.esd.ornl.gov/projects/qen/new_africa.html)
Stalagmite growth rate (mm/yr)
4
1
0.4
0.1
0.04
0.01
0.004
$r^2 = 0.12$
$p = 0.002$
← Drier Wetter →
Zero growth with zero atmospheric precipitation
100
400
1000
1350 1600 1800
4000
10000
Modern average annual atmospheric precipitation (mm)

Figure 13. Geographic extent of the AHP in equatorial Africa. Adapted Figure 1 from Liu et al. (2017) showing commonly cited African Humid Period sites. Orange circles mark terrestrial sites and blue circles mark marine sites. The positions of the Inter-Tropical Convergence Zone (ITCZ, orange lines) and the Congo Air Boundary (CAB, blue lines) for Northern Hemisphere summer (JJA: June, July, August, solid lines) and winter (DJF: December, January, February, dashed lines) modified from Willis et al. (2013). The figure has been adapted to show this new AHP site in central equatorial Africa. The position of Matupi Cave on the eastern edge of central equatorial Africa (Fig. 4) serves as a more western record of the AHP in equatorial Africa.

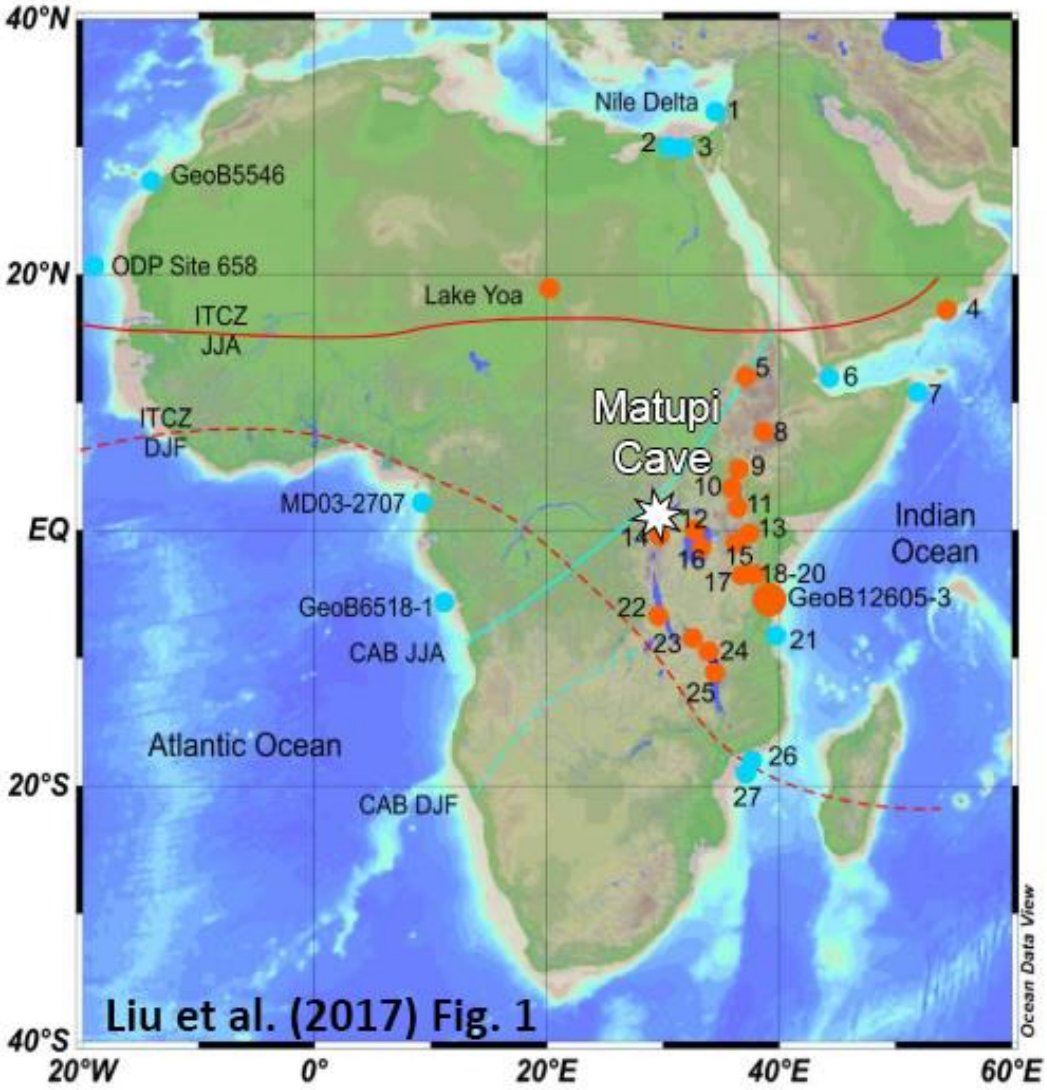
40°N
20°N
EQ
20°S
40°S
20°W
0°
20°E
40°E
60°E
Nile Delta
1
2
3
GeoB5546
ODP Site 658
Lake Yoa
ITCZ
JJA
4
5
6
7
Matupi
Cave
ITCZ
DJF
8
9
10
11
12
13
14
15
16
17
18-20
MD03-2707
Indian
Ocean
GeoB12605-3
GeoB6518-1
22
23
24
21
CAB JJA
25
Atlantic Ocean
26
27
CAB DJF
Liu et al. (2017) Fig. 1
Ocean Data View

Figure 14. Timing of AHP records from equatorial Africa of various proxy types plotted by latitude. A large grey rectangle marks the AHP from ca. 5.5 kyr BP to 14.8 kyr BP. Climate events the Younger Dryas and the 8.2 ka event are marked by dashed lines. Matupi Cave, the site from this study, is the only study that uses stalagmite data. White bars labelled MAT-1 and MAT-23 indicate two Matupi stalagmites currently under study.

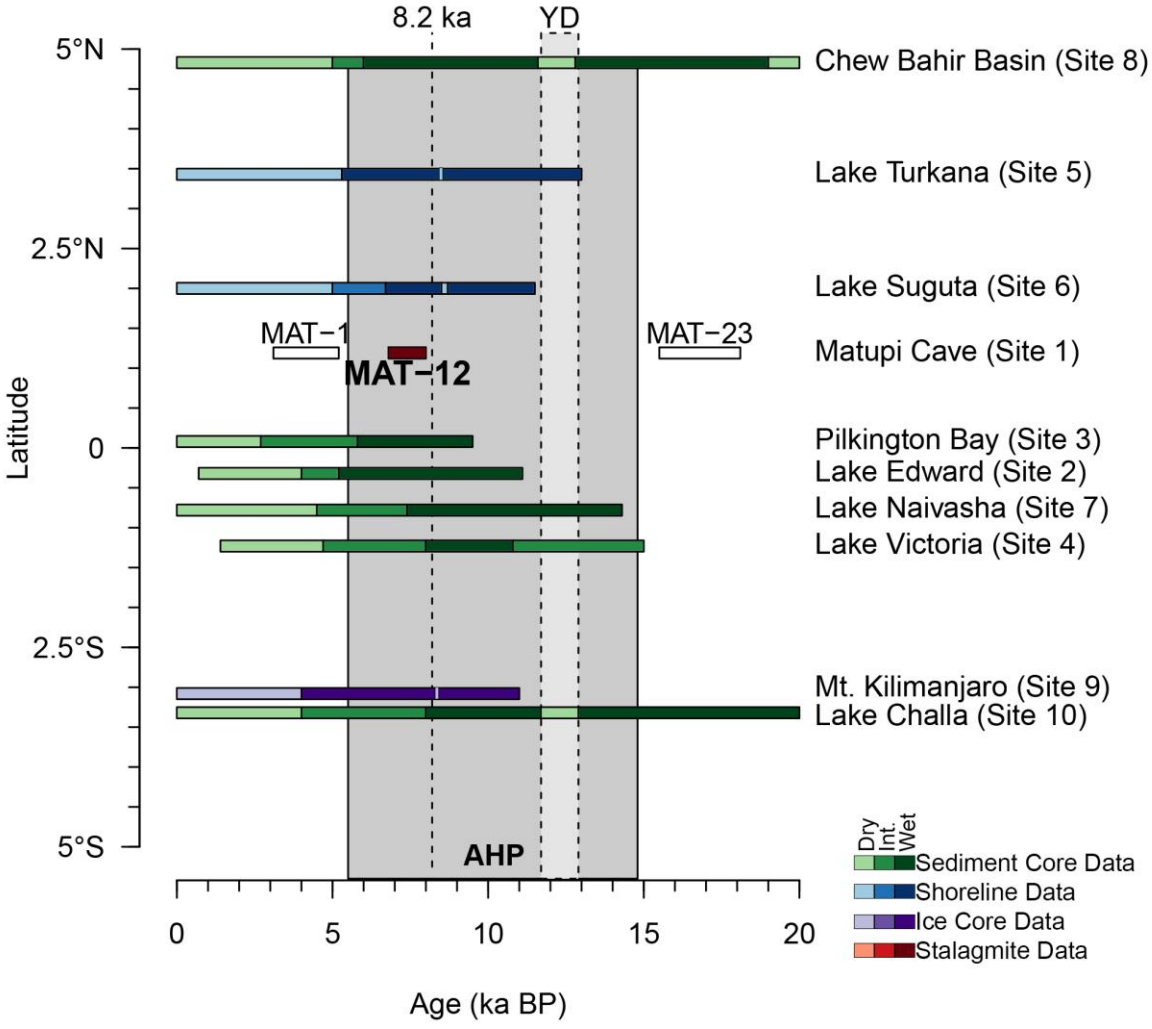
8.2 ka
YD
5°N
2.5°N
0
2.5°S
5°S
Latitude
Chew Bahir Basin (Site 8)
Lake Turkana (Site 5)
Lake Suguta (Site 6)
MAT−1
MAT−23
MAT−12
Matupi Cave (Site 1)
Pilkington Bay (Site 3)
Lake Edward (Site 2)
Lake Naivasha (Site 7)
Lake Victoria (Site 4)
Mt. Kilimanjaro (Site 9)
Lake Challa (Site 10)
AHP
Dry
Int.
Wet
Sediment Core Data
Shoreline Data
Ice Core Data
Stalagmite Data
0
5
10
15
20
Age (ka BP)

Figure 15. Matupi Cave stalagmites and insolation through time. Variation in seasonal insolation for February–April (green curve) and August–October (orange curve) plotted through the late-Pleistocene to present. The African Humid Period is marked by a black arrow from ca. 5.5 kyr BP to 14.8 kyr BP. Three grey bars mark the time of deposition for Stalagmite MAT-23, Stalagmite MAT-12, and Stalagmite MAT-1. Stalagmite MAT-12 is the specimen in this study.

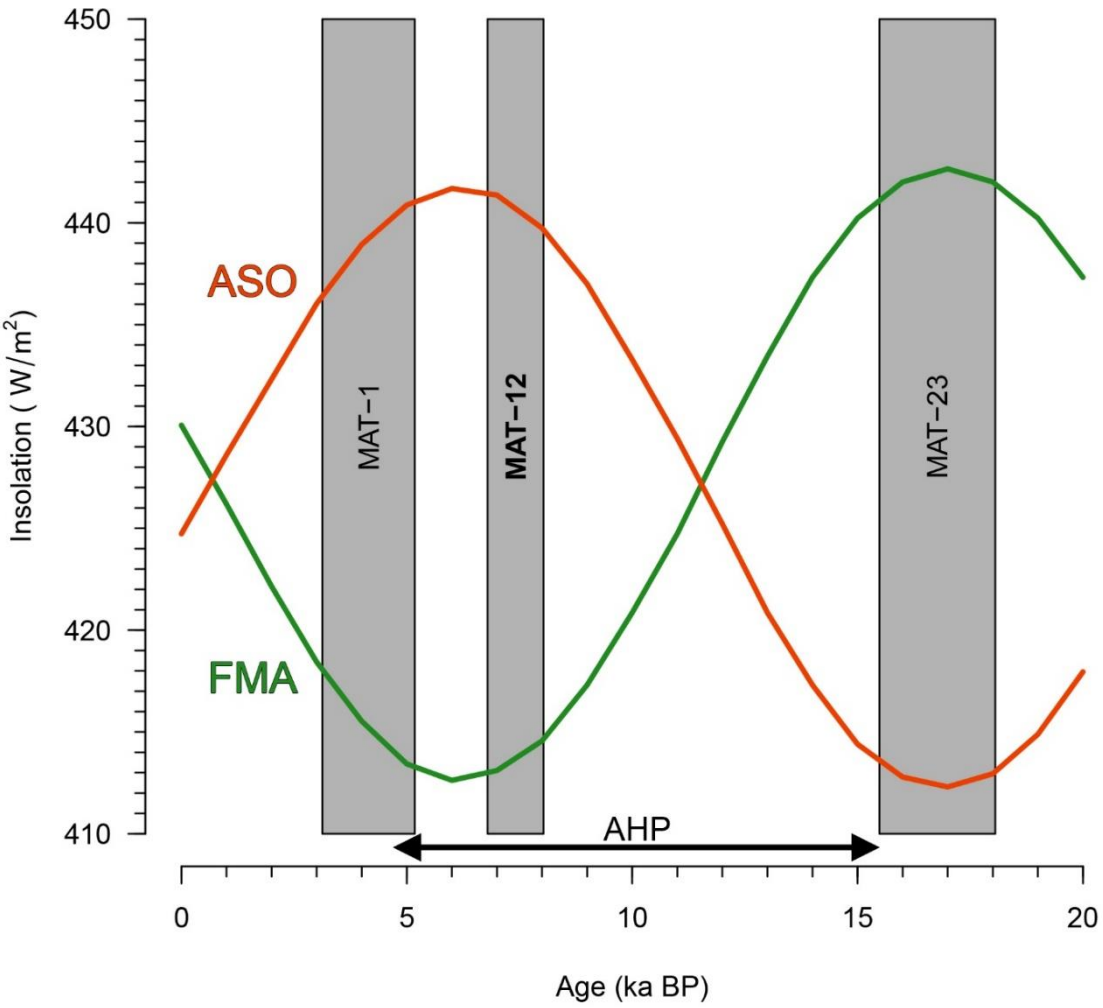
450
440
430
420
410
Insolation (W/m^2)
ASO
FMA
MAT−1
MAT−12
MAT−23
AHP
0
5
10
15
20
Age (ka BP)

CHAPTER 6: CONCLUSION

This multi-proxy record from Stalagmite MAT-12 from Matupi Cave in central equatorial Africa combines the results from multiple petrographic and isotopic proxies to suggest the environment near Matupi Cave experienced wet conditions during its deposition from ca. 6800–8050 yr BP during the height the African Humid Period in equatorial Africa. The petrographic data and isotopic data suggest reconstructions that are detailed in a way that may not be significant to AHP studies in equatorial Africa as a whole. This new study improves the current understanding of the AHP by suggesting three chief conclusions:

1) Stalagmite MAT-12 confirms that the AHP is apparent farther west in equatorial Africa than previously recognized, and thus in wetter regions of Africa (rather than the drier environments typical of eastern equatorial Africa AHP sites).
2) The deposition of Stalagmite MAT-12 at the height of the AHP may suggest that in wetter, tropical regions, the AHP is only recognizable during pronounced wet events.
3) The deposition of Stalagmite MAT-12, along with two other Matupi stalagmites still under analysis, occurred during maxima in insolation during the equinoctial seasons of rainfall (February–April and August–October), illustrating the unique dynamics of equatorial climate.

REFERENCES

Adkins, J.F., deMenocal, P., Eshel, G., 2006. The "African humid period" and the record of marine upwelling from excess (230)Th in Ocean Drilling Program Hole 658C. Paleocean. 21, PA4203.

Baldini, J.U.L., McDermott, F., Baker, A., Baldini, L.M., Mattey, D.P., Railsback, L.B., 2005. Biomass effects on stalagmite growth and isotope ratios: a 20th century analogue from Wiltshire, England. Earth Planet. Sci. Lett. 240, 486–494.

Barker, P.A., Hurrell, E.R., Leng, M.J., Wolff, C., Cocquyt, C., Sloane, H.J., Verschuren, D., 2011. Seasonality in equatorial climate over the past 25 k.y. revealed by oxygen isotope records from Mount Kilimanjaro. Geology 39, 1111-1114.

Beck, H.E., Zimmermann, N.E., McVicar, T.R., Vergopolan, N., Berg, A., Wood, E.F., 2018. Present and future Köppen-Geiger climate classification maps at 1-km resolution. Sci. Data 5, 1-12.

Berger, A., Loutre, M.F., 1991. Insolation values for the climate of the last 10 million years. Quat. Sci. Rev. 10, 297–317.

Berke, M.A., Johnson, T.C., Werne, J.P., Grice, K., Schouten, S., Sinninghe Damsté, J.S., 2012. Molecular records of climate variability and vegetation response since the Late Pleistocene in the Lake Victoria basin, East Africa. Quat. Sci. Rev. 55, 59–74.

Berke, M.A., Johnson, T.C., Werne, J.P., Livingstone, D.A., Grice, K., Schouten, S., Sinninghe Damsté, J.S., 2014. Characterization of the last deglacial transition in tropical East Africa: Insights from Lake Albert. Palaeogeogr. Palaeoclimatol. Palaeoecol. 409, 1–8.

Bischoff, J.L., 1968. Catalysis, inhibition, and the calcite-aragonite problem. II. The vaterite aragonite transformation. Am. J. Sci. 266, 80–90.

Bischoff, J.L., Fyfe, W.S., 1968. Catalysis, inhibition, and the calcite-aragonite problem. I. The aragonite-calcite transformation. Am. J. Sci. 266, 65–79.

Brook, G.A., Burney, D.A., Cowart, J.B., 1990. Paleoenvironmental data for Ituri, Zaire, from sediments in Matupi Cave, Mt. Hoyo. Virginia Museum of Natural History Memoirs 1, 49–70.

Brook, G.A., Ellwood, B.B., Railsback, L.B., Cowart, J.B., 2006. A 164 ka record of environmental change in the American Southwest from a Carlsbad Cavern speleothem. Palaeogeogr. Palaeoclimatol. Palaeoecol. 237, 483–507.

Brook, G.A., Rafter, M.A., Railsback, L.B., Sheen, S.W., Lundberg, J., 1999. A high-resolution proxy record of rainfall and ENSO since AD 1550 from layering in stalagmites from Anjohibe Cave, Madagascar. The Holocene 9, 695–705.

Brook, G.A., Scott, L., Railsback, L.B., Goddard, E.A., 2010. A 35 ka pollen and isotope record of environmental change along the southern margin of the Kalahari from a stalagmite and animal dung deposits in Wonderwerk Cave, South Africa. J. Arid Environ. 74, 870–884.

Burns, S.J., Fleitmann, D., Mudelsee, M., Neff, U., Matter, A., Mangini, A., 2002. A 780 year annually resolved record of Indian Ocean monsoon precipitation from a speleothem from south Oman. J. Geophys. Res. Atmos. 107, D20.

Burns, S.J., Godfrey, L.R., Faina, P., McGee, D., Hardt, B., Ranivoharimanana, L., Randrianasy, J., 2016. Rapid human-induced landscape transformation in Madagascar at the end of the first millennium of the Common Era. Quat. Sci. Rev. 134, 92–99.

Burrough, S.L., Thomas, D.S.G., 2013. Central southern Africa at the time of the African Humid Period: a new analysis of Holocene palaeoenvironmental and palaeoclimate data. Quat. Sci. Rev. 80, 29–46.

Cabrol, P., Coudray, J., 1982. Climatic fluctuations influence the genesis and diagenesis of carbonate speleothems in southwestern France. Natl. Spel. Soc. Bul. 44, 112–117.

Caddeo, G.A., De Waele, J., Frau, F., Railsback, L.B., 2011. Trace element and stable isotope data from a flowstone in a natural cave of the mining district of SW Sardinia (Italy): evidence for Zn2+-induced aragonite precipitation in comparatively wet climatic conditions. Int. J. Speleol. 40, 181–190.

Cai, B., Pumijumnong, N., Tan, M., Muangsong, C., Kong, X., Jiang, X., Nan, S., 2010. Effects of intraseaonsal variation of summer monsoon rainfall on stable isotope and growth rate of a stalagmite from northwestern Thailand. J. Geophys. Res. 115, D21104.

Collister, J.W., Rieley, G., Stern, B., Eglinton, G., Fry, B., 1994. Compound-specific δ13C analyses of leaf lipids from plants with differing carbon dioxide metabolisms. Org. Geochem. 21, 619–627.

Costa, K., Russell, J., Konecky, B., Lamb, H., 2014. Isotopic reconstruction of the African Humid Period and Congo Air Boundary migration at Lake Tana, Ethiopia. Quat. Sci. Rev. 83, 58–67.

Cheng, H., Edwards, L.R., Shen, C. C., 2013. Improvements in 230Th dating, 230Th and 234U half-life values, and U-Th isotopic measurements by multi-collector inductively coupled plasma mass spectrometry. Earth and Planetary Science Letters 371–372, 82–91.

Clark, I.D., Fritz, P., 1997. Environmental Isotopes in Hydrogeology. Lewis Publishers.

Cross, M., McGee, D., Broecker, W.S., Quade, J., Shakun, J.D., Cheng, H., Lu, Y., Edwards, R.L., 2015. Great Basin hydrology, paleoclimate, and connections with the North Atlantic: a speleothem stable isotope and trace element record from Lehman Caves, NV. Quat. Sci. Rev. 127, 186–198.

Cruz, F.W., Burns, S.J., Karmann, I., Sharp, W.D., Vuille, M., Ferrari, J.A., 2006. A stalagmite record of changes in atmospheric circulation and soil processes in the Brazilian subtropics during the Late Pleistocene. Quat. Sci. Rev. 25, 2749–2761.

Cuthbert, M.O., Baker, A., Jex, C.N., Graham, P.W., Treble, P.C., Andersen, M.S., Acworth, R.I., 2014. Drip water isotopes in semi-arid karst: implications for speleothem paleoclimatology. Earth Planet. Sci. Lett. 395, 194–204.

Dansgaard, W., 1964. Stable isotopes in precipitation. Tellus 16, 436–468.

demenocal, P., Ortiz, J., Guilderson, T., Adkins, J., Sarnthein, M., Baker, L., Yarusinsky, M., 2000. Abrupt onset and termination of the African Humid Period: rapid climate responses to gradual insolation forcing. Quat. Sci. Rev. 19, 347–361.

Deininger, M., Fohlmeister, J., Scholz, D., Mangini, M., 2012. Isotope disequilibrium effects: the influence of evaporation and ventilation effects on the carbon and oxygen isotope composition of speleothems - a model approach. Geochim. Cosmochim. Acta 96, 57–79.

Denniston, R.F., Asmerom, Y., Lachniet, M., Polyak, V.J., Hope, P., An, N., Rodzinyak, K., Humphreys, W.F., 2013. A last glacial maximum through middle Holocene stalagmite record of coastal Western Australia climate. Quat. Sci. Rev. 77:101–112.

Drake, N.A., Blench, R.M., Armitage, S.J., Bristow, C.S., White, K.H., 2011. Ancient watercourses and biogeography of the Sahara explain the peopling of the desert. Proc. Natl. Acad. Sci. USA 108, 458–462.

Dreybrodt, W., 1999. Chemical kinetics, speleothem growth and climate. Boreas 28, 347–356.

Dreybrodt, W., Franke, H.W., 1987.Wachstumsgeschwindigkeiten und Durchmesser von Kerzenstalagmiten. Die Höhle 38, 1–6.

Dreybrodt, W., Scholz, D., 2011. Climatic dependence of stable carbon and oxygen isotope signals recorded in speleothems: from soil water to speleothem calcite. Geochim. Cosmochim. Acta 75, 734–752.

Dreybrodt, W., 2016. Comment on "Stoll H. et al. (2015): Interpretation of orbital scale variability in mid-latitude speleothem d18O: significance of growth rate controlled kinetic fractionation effects. Quat. Sci. Rev. 127, 215e228. Quat. Sci. Rev. 142, 179–181.

Dutt, S., Gupta, A.K., Clemens, S., Cheng, H., Singh, R.K., Kathyat, G., Edwards, R.L., 2015. Abrupt changes in Indian summer monsoon strength during 33,800 to 5500 years B.P. Geophys. Res. Lett. 42, 5526-5532.

Dykoski, C.A., Edwards, R.L., Cheng, H., Yuan, D., Cai, Y., Zhang, M., Lin, Y., Qing, J., An, Z., Revenaugh, J., 2005. A high-resolution, absolute-dated Holocene and deglacial Asian monsoon record from Dongge Cave, China. Earth Planet. Sci. Lett. 233, 71–86.

Edwards, R.L., Chen, J.H., Wasserburg, G.J., 1987. 238 U-234 U-230 Th-232 Th systematics and the precise measurement of time over the past 500,000 years, Earth Planet. Sci. Lett. 81, 175-192.

Fairchild, I.J., McMillan, E.A., 2007. Speleothems as indicators of wet and dry periods. Int. J. Speleol. 36, 9–74.

Fairchild, I.J., Treble, P.C., 2009. Trace elements in speleothems as recorders of environmental change. Quat. Sci. Rev. 28, 449–468.

Fairchild, I. J., Baker, A. 2012. Speleothem science. From process to past environments. Wiley Blackwell, Chichester.

Fischbeck, R., 1976. Mineralogie und Geochemie carbonatischer Ablagerungen in europäischen Höhlenein Beitrag zur Bildung und Diagenese von Speleothemen. N. Jb. Mineral. (Abh.) 126, 269–291.

Fleitmann, D., Burns, S.J., Mangini, A., Mudelsee, M., Kramers, J., Villa, I., Neff, U., Al-Subbary, A.A., Buettner, A., Hippler, D., Matter, A., 2007. Holocene ITCZ and Indian monsoon dynamics recorded in stalagmites from Oman and Yemen (Socotra). Quat. Sci. Rev. 26, 170–188.

Foerster, V., Junginger, A., Langkamp, O., Gebru, T., Asrat, A., Umer, M., Lamb, H.F., Wennrich, V., Rethemeyer, J., Nowaczyk, N., Trauth, M.H., Schaebitz, F., 2012. Climatic change recorded in the sediments of the Chew Bahir basin, southern Ethiopia, during the last 45,000 years. Quat. Int. 274, 25–37.

Forman, S.L., Wright, D.K., Bloszies, C., 2014. Variations in water level for Lake Turkana in the past 8500 years near Mt. Porr, Kenya and the transition from the African Humid Period to Holocene aridity. Quat. Sci. Rev. 97, 84–101.

Frisia, S., Borsato, A., Fairchild, I.J., McDermott, F., Selmo, E.M., 2002. Aragonite–calcite relationships in speleothems (Grotte de Clamouse, France): environment, fabrics, and carbonate geochemistry. J. Sediment. Res. 772, 687–699.

Frisia, S., Fairchild, I.J., Fohlmeister, J., Miorandi, R., Spötl, C., Borsato, A., 2011. Carbon mass-balance modelling and carbon isotope exchange processes in dynamic caves. Geochim. Cosmochim. Acta 75, 380–400.

Garcin, Y., Melnick, D., Strecker, M.R., Olago, D., Tiercelin, J.J., 2012. East African mid-Holocene wet–dry transition recorded in palaeo-shorelines of Lake Turkana, northern Kenya Rift. Earth Planet. Sci. Lett. 331-332, 322-334.

Gasse, F., 2002. Diatom-inferred salinity and carbonate oxygen isotopes in Holocene waterbodies of the western Sahara and Sahel (Africa). Quat. Sci. Rev. 21, 737–767.

Genty, D., Baker, A., Massault, M., Proctor, C., Gilmour, M., Pons-Branchu, E., Hamelin, B., 2001. Dead carbon in stalagmites: carbonate bedrock paleodissolution vs. ageing of soil organic matter: implications for 13C variations in speleothems. Geochim. Cosmochim. Acta 65, 3443–3457.

Genty, D., Blamart, D., Ouahdi, R., Gilmour, M., Baker, A., Jouzel, J., Van-Exter, S., 2003. Precise dating of Dansgaard-Oeschger climate oscillations in western Europe from stalagmite data. Nature 421, 833–837.

Genty, D., Blamart, D., Ghaleb, B., Plagnes, V., Causse, C., Bakalowicz, M., Zouari, K., Chkir, N., Hellstrom, J., Wainer, K., Bourges, F., 2006. Timing and dynamics of the last deglaciation from European and North African δ13C stalagmite profiles — comparison with Chinese and South Hemisphere stalagmites. Quat. Sci. Rev. 25, 2118–2142.

González, L.A., Lohmann, K.C., 1988. Controls on mineralogy and composition of spelean carbonates: Carlsbad Caverns, New Mexico. In: James, N.P., Choquette, P.W. (Eds.), Paleokarst. Springer-Verlag, New York, pp. 81–101.

Harris, I., Jones, P.D., Osborn, T.J., Lister, D.H., 2014. Updated high-resolution grids of monthly climatic observations — the CRU Ts3.10 Dataset. Int. J. Climatol. 34, 623-642.

Haug, G.H., Hughen, K.A., Sigman, D.M., Peterson, L.C., Röhl, U., 2001. Southward Migration of the Intertropical Convergence Zone through the Holocene. Science 293, 1304-1308.

Hély, C., Braconnot, P., Watrin, J., Zheng, W., 2009. Climate and vegetation: Simulating the African humid period. Comptes Rendus Geosci. 341, 671–688.

Hendy, C., 1971. The isotopic geochemistry of speleothems I: the calculation of the effects of different modes of formation on the isotopic composition of speleothems and their applicability as palaeoclimatic indicators. Geochimica et Cosmochimica Acta 35, 801–824.

Hesterberg, R., Siegenthaler, U., 1991. Production and stable isotopic composition of CO2 in a soil near Bern, Switzerland. Tellus Ser. B Chem. Phys. Meteorol. 43, 197–205.

Hill, C., Forti, P., 1997. Cave Minerals of the World. National Speleological Society, Huntsville, AL (463 p).

Hoefs, J., 2009. Stable Isotope Geochemistry. sixth ed. Springer, Berlin (293 p).

Holmes, J., Hoelzmann, P., 2017. The Late Pleistocene-Holocene African Humid Period as Evident in Lakes. Oxford Research Encyclopedia of Climate Science, 1-44.

Johnson, K.R., Hu, C.Y., Belshaw, N.S., Henderson, G.M., 2006. Seasonal trace-element and stable-isotope variations in a Chinese speleothem: the potential for high-resolution paleomonsoon reconstruction. Earth Planet. Sci. Lett. 244, 394–407.

Jung, S.J.A., Davies, G.R., Ganssen, G.M., Kroon, D., 2004. Stepwise Holocene aridification in NE Africa deduced from dust-borne radiogenic isotope records. Earth Planet. Sci. Lett. 221, 27–37.

Junginger, A., Roller, S., Olaka, L.A., Trauth, M.H., 2014. The effects of solar irradiation changes on the migration of the Congo Air Boundary and water levels of paleo-Lake Suguta, Northern Kenya Rift, during the African Humid Period (15–5ka BP). Palaeogeogr. Palaeoclimatol. Palaeoecol. 396, 1–16.

Kato, H., Yamada, T., 2016. Controlling factors in stalagmite oxygen isotopic composition and the paleoprecipitation record for the last 1,100 years in Northeast Japan. Geochem. J. 50, 1-6.

Kaufmann, G., 2003. Stalagmite growth and palaeo-climate: the numerical perspective. Earth Planet Sci. Lett. 214, 251–266.

Kaufmann, G., Dreybrodt, W., 2004. Stalagmite growth and palaeo-climate: an inverse approach. Earth Planet Sci. Lett. 224, 529–545.

Kendall, R.L., 1969. An ecological history of the Lake Victoria basin. Ecol. Monogr. 39, 121–176.

Kim, S. T., O'Neil, J. R., Hillaire-Marcel, C., Mucci A., 2007. Oxygen isotope fractionation between synthetic aragonite and water: Influence of temperature and $Mg2^{+}$ concentration. Geochimica et Cosmochimica Acta 71, 4704–4715.

Koster, R.D., Devalpine, D.P., Jouzel, J., 1993. Continental water recycling and H2O concentrations. Geophys. Res. Lett. 20, 2215–2218.

Kröpelin, S., Verschuren, D., Lézine, A.M., Eggermont, H., Cocquyt, C., Francus, P., Cazet, J.P., Fagot, M., Rumes, B., Russell, J.M., Darius, F., Conley, D.J., Schuster, M., Von Suchodoletz, H., Engstrom, D.R., 2008. Climate-Driven Ecosystem Succession in the Sahara: The Past 6000 Years. Science 320, 765-768.

Kutzbach, J.E., Liu, Z., 1997. Response of the African Monsoon to Orbital Forcing and Ocean Feedbacks in the Middle Holocene. Science 278, 440-443.

Lachniet, M.S., 2009. Climatic and environmental controls on speleothem oxygen-isotope values. Quat. Sci. Rev. 28, 412–432.

Lambert, W.J., Aharon, P., 2011. Controls on dissolved inorganic carbon and $d^{13}C$ in cave waters from DeSoto Caverns: implications for speleothem delta C-13 assessments. Geochimica et Cosmochimica Acta 75 (3), 753–768.

Lauritzen, S.E., Lundberg, J., 1999. Speleothems and climate: a special issue of The Holocene. The Holocene 9, 643–647.

Lézine, A.M., Hély, C., Grenier, C., Braconnot, P., Krinner, G., 2011. Sahara and Sahel vulnerability to climate changes, lessons from Holocene hydrological data. Quat. Sci. Rev. 30, 3001–3012.

Liu, X., Rendle-Bühring, R., Kuhlmann, H., Li, A., 2017. Two phases of the Holocene East African Humid Period: Inferred from a high-resolution geochemical record off Tanzania. Earth Planet. Sci. Lett. 460, 123–134.

Liu, Z., Wang, Y., Gallimore, R., Gasse, F., Johnson, T., deMenocal, P., Adkins, J., Notaro, M., Prentice, I.C., Kutzbach, J., Jacob, R., Behling, P., Wang, L., Ong, E., 2007. Simulating the transient evolution and abrupt change of Northern Africa atmosphere-ocean-terrestrial ecosystem in the Holocene. Quat. Sci. Rev. 26, 1818–1837.

Marshall, M.H., Lamb, H.F., Huws, D., Davies, S.J., Bates, R., Bloemendal, J., Boyle, J., Leng, M.J., Umer, M., Bryant, C., 2011. Late Pleistocene and Holocene drought events at Lake Tana, the source of the Blue Nile. Glob. Planet. Change 78, 147–161.

Maitima, J.M., 1991. Vegetation Response to Climatic-Change in Central Rift-Valley, Kenya. Quat. Res. 35, 234-245.

McDermott, F., 2004. Palaeo-climate reconstruction from stable isotope variations in speleothems: a review. Quat. Sci. Rev. 23, 901–918.

McIntosh, S.K., McIntosh, R.J., 1983. Current Directions in West African Prehistory. Annu. Rev. Anthropol. 12, 215–258.

McMillan, E.A., Fairchild, I.J., Frisia, S., Borsato, A., McDermott, F., 2005. Annual trace element cycles in calcite–aragonite speleothems: evidence of drought in the western Mediterranean 1200–1100 yr BP. J. Quat. Sci. 20, 423–433.

Meyer, K.W., Feng, W., Breecker, D.O., Banner, J.L., Guilfoyle, A., 2014. Interpretation of speleothem calcite δ13C variations: evidence from monitoring soil CO2, drip water, and modern speleothem calcite in central Texas. Geochim. Cosmochim. Acta 142: 281–298.

Mickler, P.J., Banner, J.L., Stern, L., Asmerom, Y., Edwards, R.L., Ito, E., 2004. Stable isotope variations in modern tropical speleothems: evaluating equilibrium vs. kinetic isotope effects. Geochim. Cosmochim. Acta 68, 4381–4393.

Mickler, P.J., Stern, L.A., Banner, J.L., 2006. Large kinetic isotope effects in modern speleothems. Geol. Soc. Am. Bull. 118, 65–81.

Middleton, J., Middleton, V., 2002. Karst and caves of Madagascar. Cave Karst Sci. 29, 13–20.

Moore, G.W., 1956. Aragonite speleothem as indicators of paleotemperature. Am. J. Sci. 254, 746–753.

Moreno, A., Stoll, H., Jimenez-Sanchez, M., Cacho, I., Valero-Garces, B., Ito, E., Edwards, R.L., 2010. A speleothem record of glacial (25–11.6 kyr BP) rapid climatic changes from northern Iberian Peninsula. Glob. Planet. Chang. 71:218–231.

Mühlinghaus, C., Scholz, D., Mangini, A., 2007. Modelling stalagmite growth and $\delta^{13}C$ as a function of drip interval and temperature. Geochem. Cosmochim. Acta 71, 2780–2790.

Murray, J.W., 1954. The deposition of calcite and aragonite in caves. J. Geol. 62, 481–492.

Paul, D., Skrzypek, G., 2007. Assessment of carbonate-phosphoric acid analytical technique performed using GasBench II in continuous flow isotope ratio mass spectrometry. International Journal of Mass Spectrometry 262, 180–186.

Pobeguin, T., 1965. Sur les concretions calcaires observées dans la Grotte de Moulis (Ariège). CR Somm. Soc. Géol. Fr. 241, 1791–1793.

Proctor, C.J., Baker, A., Barnes, W.L., Gilmour, M.A., 2000. A thousand year speleothem proxy record of North Atlantic climate from Scotland. Clim. Dynam. 16, 815-820.

Quade, J., 2004. Isotopic records from groundwater and cave speleothem calcite in North America. In: Gillespie, A., Porter, S.C., Atwater, B.F. (Eds.), Developments in Quaternary Science. Elsevier Science, New York, pp. 205–219.

Railsback, L.B., Brook, G.A., Chen, J., Kalin, R., Fleisher, C.J., 1994. Environmental controls on the petrology of a Late Holocene speleothem from Botswana with annual layers of aragonite and calcite. J. Sediment. Res. A64, 147e155.

Railsback, L.B., 2000. Atlas of speleothem microfabrics.(Available at:). www.gly.uga.edu/railsback/speleoatlas/SAindex1.html (Accessed 15 January 2016).

Railsback, L.B., 2010. Controls on the δ13C of spelean CaCO3. In: Railsback, L.B. (Ed.), Some Fundamentals of Mineralogy and Geochemistry . www.gly.uga.edu/railsback/Fundamentals/C&OIsotopesSpeleanCaCO3Controls.jpg.

Railsback, L.B., Liang, F.Y., Romani, J.R.V., Grandal-d'Anglade, A., Rodriguez, M.V., Fidalgo, L.S., Mosquera, D.F., Cheng, H., Edwards, R.L., 2011. Petrographic and isotopic evidence for Holocene long-term climate change and shorter-term environmental shifts from a stalagmite from the Serra do Courel of northwestern Spain, and implications for climatic history across Europe and the Mediterranean. Palaeogeogr. Palaeoclimatol. Palaeoecol. 305, 172–184.

Railsback, L.B., Akers, P.D., Wang, L., Holdridge, G.A., Voarintsoa, N.R.G., 2013. Layer-bounding surfaces in stalagmites as keys to better paleoclimatological histories and chronologies. Int. J. Speleol. 42, 167–180.

Railsback, L.B., Xiao, H.L., Liang, F.Y., Akers, P.D., Brook, G.A., Dennis, W.M., Lanier, T.E., Tan, M., Cheng, H., Edwards, R.L., 2014. A stalagmite record of abrupt climate change and possible Westerlies-derived atmospheric precipitation during the Penultimate Glacial Maximum in northern China. Palaeogeogr. Palaeoclimatol. Palaeoecol. 393, 30–44.

Railsback, L.B., 2018. A comparison of growth rate of late Holocene stalagmites with atmospheric precipitation and temperature, and its implications for paleoclimatology. Quat. Sci. Rev. 187, 94–111.

Railsback, L.B., Dupont, L.A., Liang, F., Brook, G.A., Burney, D.A., Cheng, H., Edwards, R.L., 2020. Relationships between climate change, human environment impact, and megafaunal extinction inferred from a 4000-year multi-proxy record from a stalagmite in northwestern Madagascar. Quat. Sci. Rev. 234, 106244.

Rasmussen, J.B.T., Polyak, V.J., Asmerom, Y., 2006. Evidence for Pacific-modulated precipitation variability during the late Holocene from the southwestern USA. Geophys. Res. Lett. 33, L08701.

Riechelmann, S., Schröder-Rtizrau, A., Wassenburg, J.A., et al., 2014. Physicochemical characteristics of drip waters: influence on mineralogy and crystal morphology of recent cave carbonate precipitates. Geochim. Cosmochim. Acta 145, 13–29.

Rieley, G., Collister, J.W., Stern, B., Eglinton, G., 1993. Gas chromatography/isotope ratio mass spectrometry of leaf wax n-alkanes from plants of differing carbon dioxide metabolisms. Rapid Commun. Mass Spectrom. 7, 488–491.

Ritchie, J.C., Eyles, C.H., Haynes, C.V., 1985. Sediment and pollen evidence for an early to mid-Holocene humid period in the eastern Sahara. Nature 314, 352-355.

Romanek, C.S., Grossman, E.L, Morse, J.W., 1992. Carbon isotopic fractionation in synthetic aragonite and calcite: Effects of temperature and precipitation rate. Geochimica et Cosmochimica Acta 56, 419–430.

Rozanski, K., Araguás-Araguás, L., Gonfiantini, R., 1993. Isotopic patterns in modern global precipitation. In: Swart, P.K., Lohmann, K.L., McKenzie, J., Savin, S. (Eds.), Climate Change in Continental Isotopic Records. Amer. Geophys. Union, pp. 1–37.

Russell, J.M., Johnson, T.C., Kelts, K.R., Lærdal, T., Talbot, M.R., 2003. An 11 000-year lithostratigraphic and paleohydrologic record from Equatorial Africa: Lake Edward, Uganda-Congo. Palaeogeogr. Palaeoclimatol. Palaeoecol. 193, 25–49.

Seneviratne, S.I., Nicholls, N., Easterling, D., Goodess, C.M., Kanae, S., Kossi, J., Luo Yali, Marengo, J., McInnes, K., Rahimi, M., Reichstein, M., Sorteberg, A., Vera, C., Zhang, X., Rusticucci, M., Semenov, V., Alexander, L.V., Allen, S., Benito, G., Cavazos, T., Clague, J., Conway, D., Della-Marta, P.M., Gerber, M., Gong, S., Goswami, B.N., Hemer, M., Huggel, C., van den Hurk, B., Kharin, V.V., Kitoh, A., Klein Tank, A.M.G., Li, G., Mason, S., McGuire, W., van Oldenborgh, G.J., Orlowsky, B., Smith, S., Thiaw, W., Velegrakis, A., Yiou, P., Zhang, T., Zhou Tianjun, Swiers, F.W., 2012. Changes in climate extremes and their impacts on the natural physical environment, in: Field, C.B., Barros, V., Stocker, T.F., Qin, D., Dokken, D.J., Ebi, K.L., Mastrandrea, M.D., Mach, K.J., Plattner, G.K., Allen, S.K., Tignor, M., Midgley, P.M. (Eds.), Managing the risks of extreme events and disasters to advance climate change adaptation a special report of Working Groups I and II of the Intergovernmental Panel on Climate Change. Cambridge University Press, New York, pp. 109-230.

Shanahan, T.M., Mckay, N.P., Hughen, K.A., Overpeck, J.T., Otto-Bliesner, B., Heil, C.W., King, J., Scholz, C.A., Peck, J., 2015. The time-transgressive termination of the African humid period. Nat. Geosci. 8, 140–144.

Shen, C.C., Edwards, R.L., Cheng, H., Dorale, J.A., Thomas, R.B., Moran, S.B., Weinstein, S.E., Edmonds, H.N., 2002. Uranium and thorium isotopic and concentration measurements by magnetic sector inductively coupled plasma mass spectrometry. Chemical Geology 185, 165–178.

Siegel, F.R., 1965. Aspects of calcium carbonate deposition in Great Onyx Cave, Kentucky. Sedimentology 4, 285–299.

Skrzypek, G., Paul, D., 2006. $\delta^{13}C$ analyses of calcium carbonate: comparison between the GasBench and elemental analyzer techniques. Rapid Communications in Mass Spectrometry 20, 2915-2920.

Sletten, H.R., Railsback, L.B., Liang, F., Brook, G.A., Marais, E., Hardt, B.F., Cheng, H., Edwards, R.L., 2013. A petrographic and geochemical record of climate change over the last 4600 years from a northern Namibia stalagmite, with evidence of abruptly wetter climate at the beginning of southern Africa's Iron Age. Palaeogeography, Palaeoclimatology, Palaeoecology 376, 149–162.

Stager, J.C., Cumming, B.F., Meeker, L.D., 2003. A 10,000-year high-resolution diatom record from Pilkington Bay, Lake Victoria, East Africa. Quat. Res. 59, 172-181.

Stoffers, P., Hecky, R. E., 1978. Late Pleistocene-Holocene evolution of the Kivu-Tanganyika Basin. Special Publication of the International Association of Sedimentologists 2, 43–55.

Suess, H.E., 1955. Radiocarbon concentration in modern wood. Science 122, 415–417.

Thompson, L.G., Mosley-Thompson, E., Davis, M.E., Henderson, K.A., Brecher, H.H., Zagorodnov, V.S., Mashiotta, T.A., Lin, P.N., Mikhalenko, V.N., Hardy, D.R., Beer, J., 2002. Kilimanjaro ice core records: evidence of Holocene climate change in tropical Africa. Science 298, 589-593.

Thrailkill, J., 1971. Carbonate deposition in Carlsbad Caverns. J. Geol. 79, 683–695.

Tierney, J.E., Russell, J.M., Huang, Y., Sinninghe Damsté, J.S., Hopmans, E.C., Cohen, A.S., 2008. Northern Hemisphere Controls on Tropical Southeast African Climate during the Past 60,000 Years. New Ser. 322, 252–255.

Tierney, J.E., Lewis, S.C., Cook, B.I., LeGrande, A.N., Schmidt, G.A., 2011a. Model, proxy and isotopic perspectives on the East African Humid Period. Earth Planet. Sci. Lett. 307, 103–112.

Tierney, J.E., Russell, J.M., Sinninghe Damste, J.S., Huang, Y., Verschuren D., 2011b. Late Quaternary behavior of the East African monsoon and the importance of the Congo Air Boundary. Quat. Sci. Rev. 30, 798-807.

Verburg, P., 2007. The need to correct for the Suess effect in the application of δ13C in sediment in autotrophic Lake Tanganyika, as a productivity proxy in the anthropocene. J. Paleolimnol. 37, 591–602.

Verschuren, D., Sinninghe Damste, J.S., Moernaut, J., Kristen, I., Blaauw, M., Fagot, M., Haug, G.H., CHALLACEA project members, 2009. Half-precessional dynamics of monsoon rainfall near the East African Equator. Nature 462, 637-641.

Voarintsoa, N.R.G., Brook, G.A., Liang, F., Marais, E., Hardt, B., Cheng, H., Edwards, R.L., Railsback, L.B., 2016. Stalagmite multi-proxy evidence of wet and dry intervals in northeastern Namibia: linkage to latitudinal shifts of the Inter-Tropical Convergence Zone and changing solar activity from AD 1400 to 1950. The Holocene 27, 384–396.

Voarintsoa, N. R. G., Wang, L., Railsback, L. B., et al. 2017. Multiple proxy analyses of a U/Th-dated stalagmite to reconstruct paleoenvironmental changes in northwestern Madagascar between 370 CE and 1300 CE. Palaeogeography, Palaeoclimatology, Palaeoecology 469, 138–155.

Voarintsoa, N.R.G., 2017. Investigating stalagmites from NE Namibia and NW Madagascar as a key to better understand local paleoenvironmental changes and implications for inter-tropical convergence zone (ITCZ) dynamics [Dissertation]. University of Georgia, 299 pp.

Wang, Y.J., Cheng, H., Edwards, R.L., An, Z.S., Wu, J.Y., Shen, C., Dorale, J.A., 2001. A High-Resolution Absolute-Dated Late Pleistocene Monsoon Record from Hulu Cave. Science 294, 2345-2348.

Wang, L., Brook, G.A., Burney, D.A., Voarintsoa, N.R.G., Liang, F., Cheng, H, Edwards, R.L., 2019. The African Humid Period, rapid climate change events, the timing of human colonization, and megafaunal extinctions in Madagascar during the Holocene: Evidence from a 2m Anjohibe Cave stalagmite. Quat. Sci. Rev. 210, 136-153.

Willis, K.J., Bennett, K.D., Burrough, S.L., Tovar, C., 2013. Determining the response of African biota to climate change: using the past to model the future. Phil. Trans. R. Soc. Lond. B, Biol. Sci. 368, 1-9.

Wong, C.I., Breecker, D.O., 2015. Advancements in the use of speleothems as climate archives. Quat. Sci. Rev. 127, 1–18.

Yadava, M.G., Ramesh, R., Pant, G.B., 2004. Past monsoon rainfall variations in Peninsular India recorded in a 331-year old speleothem. The Holocene 14, 517–524.

Yan, Y.Y., 2005. Intertropical convergence zone (ITCZ). Encyclopedia of World Climatology, J.E. Oliver, Ed., Springer, 429-432.

Zielhofer, C., von Suchodoletz, H., Fletcher, W.J., Schneider, B., Dietze, E., Schlegel, M., Schepanski, K., Weninger, B., Mischke, S., Mikdad, A., 2017. Millennial-scale fluctuations in Saharan dust supply across the decline of the African Humid Period. Quat. Sci. Rev. 171, 119–135.

APPENDIX

Table S1. Layer-bounding surface results from Stalagmite MAT-12.

Dft (mm)	Surface type	Age before surface (yr BP)	Age after surface (yr BP)	Length of hiatus (yr)
24	Type L	7025	7001	24
30	Type L	7069	7043	26
70	Type L	7250	7160	90
85	Type L & E	7331	7274	57
127	Type L*	N/A	N/A	N/A
174	Type L & E	7532	7493	39
236	Type L	7715	7695	20
283	Type L	7910	7841	69

*This surface did not result in a hiatus.

Table S2. Growth rate results from Stalagmite MAT-12. Growth rate was reconstructed using the Stalagmite MAT-12 age model (Fig. 9).

Dft (mm)	Age (yr BP)	Growth rate (mm/yr)	Amt. of accepted ages in segment
0–23.5*	6790–7001	~~0.054~~	2
26–28.1*	7025–7043	~~0.120~~	0
30.5–69*	7069–7160	~~0.424~~	2
71.5–85	7250–7274	0.556	1
86.5–173	7331–7493	0.536	5
174.1–236	7532–7695	0.380	3
236.7–279.5	7715–7841	0.339	3
283.4–334.8	7910–8034	0.416	2

*Growth rates before 71.5 mm dft (i.e., from the left flank) omitted from study results.

Table S3. X-ray diffraction (XRD) results from Stalagmite MAT-12. XRD patterns were used to reconstruct mineralogy, expressed here as percent aragonite (%) when 100 % is a sample entirely composed of aragonite, 50 % is a sample composed of equal parts aragonite and calcite, and 0 % is a sample entirely composed of calcite.

Dft (mm)	Sample	Age (yr BP)	Net area aragonite (A)	Net area calcite (C)	A/(A+C)	Percent aragonite
23.0	MAT12-XRD15	6991	7.345	1.396	0.84	99.7
36.0	MAT12-XRD14	7082	6.230	1.370	0.82	99.5
63.0	MAT12-XRD13	7145	6.991	2.931	0.70	98.2
92.0	MAT12-XRD5	7342	4.714	1.482	0.76	99.0
123.0	MAT12-XRD12	7400	6.501	1.684	0.79	99.4
155.0	MAT12-XRD11	7459	6.652	1.153	0.85	99.8
177.0	MAT12-XRD4	7539	2.005	15.850	0.11	46.0
204.5	MAT12-XRD3	7612	5.388	2.098	0.72	98.7
211.0	MAT12-XRD10	7629	5.459	6.272	0.47	91.6
233.5	MAT12-XRD9	7688	2.410	20.400	0.11	46.0
260.0	MAT12-XRD8	7784	6.664	1.113	0.86	99.8
272.0	MAT12-XRD7	7819	0.053	25.770	0.00	0.0
289.5	MAT12-XRD2	7925	-0.204	24.110	-0.01	0.0
301.0	MAT12-XRD6	7952	0.009	24.760	0.00	0.0
321.0	MAT12-XRD1	8000	6.723	0.346	0.95	100.0

Table S4. Layer-specific width results from Stalagmite MAT-12. Results are separated by analyst (LAD = Dupont and LBR = Railsback).

Analyst: LBR		
Dft (mm)	Age at position (yr BP)	LSW (mm)
85	7274	32.8
94	7345	31.4
139	7429	32.5
150	7450	36.6
160	7469	38.9
173	7493	36.3
189.5	7572	31.3
206	7616	36.8
224	7663	38.2
236	7695	38.8
242	7731	42.1
250	7754	46.4
267	7805	48.3
278	7837	51.6
287	7919	47
309	7972	37.4
Analyst: LAD		
Dft (mm)	Age at position (yr BP)	LSW (mm)
85	7274	29.9
88.5	7335	28.8
107	7370	27.5
127.9	7409	23.7
139	7429	27.9
145	7441	31.5
149	7448	33
172.5	7492	36
179.9	7547	33
189	7571	27.7
197.4	7593	30
206	7616	34
223.5	7662	39.3
236	7695	35.3
258	7778	41.4
268.5	7809	42.5
276.3	7832	40.5
286.6	7918	41.4
309	7972	32.7

Table S5. Stable isotope results from Stalagmite MAT-12. An asterisk (*) indicates a sample that was lost due to autosampler error.

Dft (mm)	Sample	Age (yr BP)	$\delta^{18}O$ (uncorrected)	$\delta^{18}O$ (corrected)	$\delta^{13}C$ (uncorrected)	$\delta^{13}C$ (corrected)
12.2	MAT12-142	6790	-3.3	-3.4	-9.5	-11.2
13.4	MAT12-141	6812	-2.9	-3.0	-7.8	-9.5
16.3	MAT12-140	6866	-3.3	-3.4	-8.2	-9.9
18.5	MAT12-139	6907	-2.7	-2.8	-7.5	-9.2
21.8	MAT12-138	6969	-2.9	-2.9	-8.4	-10.0
23.5	MAT12-137	7001	-2.5	-2.6	-8.2	-9.9
26.0	MAT12-136	7025	-3.5	-3.6	-9.3	-11.0
28.1	MAT12-135	7043	-4.0	-4.1	-8.9	-10.6
30.5	MAT12-134	7069	-3.1	-3.1	-8.7	-10.4
32.5	MAT12-133	7073	-2.8	-2.8	-8.2	-9.9
34.3	MAT12-132	7078	-4.2	-4.3	-8.2	-9.9
37.5	MAT12-131	7085	-3.1	-3.1	-7.9	-9.6
39.0	MAT12-130	7089	-4.4	-4.4	-10.2	-11.9
41.7	MAT12-129	7095	-3.9	-4.0	-10.5	-12.2
44.0	MAT12-128	7101	-2.9	-3.0	-10.4	-12.0
46.2	MAT12-127	7106	-3.5	-3.6	-9.0	-10.7
48.1	MAT12-126	7110	-3.6	-3.7	-9.5	-11.2
50.5	MAT12-125	7116	-3.2	-3.2	-9.1	-10.8
52.3	MAT12-124	7120	-3.8	-3.8	-9.5	-11.1
54.0	MAT12-123	7124	-3.1	-3.2	-7.3	-9.0
56.7	MAT12-122	7131	-4.1	-4.1	-8.5	-10.1
59.8	MAT12-121	7138	-4.6	-4.7	-9.4	-11.1
62.5	MAT12-120	7144	-3.8	-3.9	-9.5	-11.2
64.4	MAT12-119	7149	-3.9	-4.0	-9.7	-11.4
66.0	MAT12-118	7152	-2.6	-2.7	-7.7	-9.4
67.1	MAT12-117*	N/A	N/A	N/A	N/A	N/A
69.0	MAT12-116	7160	-3.4	-3.5	-7.2	-8.9
71.5	MAT12-115	7250	-4.2	-4.3	-8.5	-10.2
73.5	MAT12-114	7253	-2.8	-2.8	-8.5	-10.1
74.9	MAT12-113	7256	-2.6	-2.7	-8.4	-10.0
76.9	MAT12-112	7259	-2.5	-2.5	-8.3	-10.0
77.0	MAT12-111	7260	-3.1	-3.1	-8.5	-10.2
78.0	MAT12-110	7261	-3.9	-3.9	-8.9	-10.6
80.3	MAT12-109	7266	-3.2	-3.3	-8.2	-9.9
82.0	MAT12-108	7269	-2.9	-3.0	-8.5	-10.2
84.0	MAT12-107	7272	-4.3	-4.4	-8.9	-10.6

Dft (mm)	Sample	Age (yr BP)	$\delta^{18}O$ (uncorrected)	$\delta^{18}O$ (corrected)	$\delta^{13}C$ (uncorrected)	$\delta^{13}C$ (corrected)
86.5	MAT12-106	7331	-4.3	-4.4	-9.3	-10.9
88.3	MAT12-105	7335	-4.4	-4.5	-8.7	-10.4
90.5	MAT12-104	7339	-3.0	-3.1	-8.0	-9.7
88.3	MAT12-105	7335	-4.4	-4.5	-8.7	-10.4
93.0	MAT12-103	7344	-3.1	-3.2	-9.1	-10.8
95.5	MAT12-102	7348	-2.7	-2.7	-8.7	-10.4
98.1	MAT12-101	7353	-4.7	-4.8	-9.7	-11.4
100.5	MAT12-100	7358	-3.7	-3.8	-8.7	-10.3
102.9	MAT12-99	7362	-3.3	-3.4	-9.4	-11.1
105.2	MAT12-98	7366	-3.3	-3.4	-8.7	-10.4
108.1	MAT12-97	7372	-3.8	-3.9	-9.2	-10.9
110.6	MAT12-96	7376	-4.5	-4.6	-9.4	-11.1
113.4	MAT12-95	7382	-4.0	-4.1	-9.4	-11.1
116.0	MAT12-94	7387	-3.0	-3.1	-8.4	-10.1
119.3	MAT12-93	7393	-3.0	-3.1	-8.3	-10.0
122.0	MAT12-92	7398	-4.1	-4.2	-9.4	-11.1
125.0	MAT12-91	7403	-4.1	-4.2	-8.8	-10.5
128.3	MAT12-90	7409	-2.9	-2.9	-7.0	-8.7
130.7	MAT12-89	7414	-3.7	-3.8	-7.5	-9.2
133.0	MAT12-88	7418	-4.0	-4.1	-8.2	-9.9
135.0	MAT12-87	7422	-4.1	-4.1	-10.2	-11.9
137.5	MAT12-86	7427	-3.3	-3.4	-9.3	-11.0
140.0	MAT12-85	7431	-3.4	-3.5	-9.0	-10.7
142.4	MAT12-84	7436	-3.6	-3.6	-9.5	-11.2
145.3	MAT12-83	7441	-4.0	-4.1	-9.4	-11.1
148.1	MAT12-82	7446	-4.0	-4.1	-8.7	-10.4
151.0	MAT12-81	7452	-3.4	-3.4	-9.6	-11.3
153.7	MAT12-80	7457	-3.6	-3.7	-10.1	-11.8
155.5	MAT12-79	7460	-4.2	-4.3	-10.0	-11.7
158.1	MAT12-78	7465	-3.7	-3.8	-10.3	-11.8
160.3	MAT12-77	7469	-3.1	-3.2	-9.8	-11.3
162.4	MAT12-76	7473	-4.2	-4.2	-10.0	-11.4
164.1	MAT12-75	7476	-4.4	-4.4	-10.2	-11.5
166.2	MAT12-74	7480	-4.2	-4.3	-9.6	-10.8
168.2	MAT12-73	7484	-4.3	-4.4	-10.4	-11.6
170.0	MAT12-72	7487	-4.1	-4.2	-9.8	-10.8
172.1	MAT12-71	7491	-3.5	-3.5	-9.3	-10.3
174.1	MAT12-70	7532	-3.2	-3.2	-7.8	-8.7

Dft (mm)	Sample	Age (yr BP)	$\delta^{18}O$ (uncorrected)	$\delta^{18}O$ (corrected)	$\delta^{13}C$ (uncorrected)	$\delta^{13}C$ (corrected)
175.9	MAT12-69	7537	-3.8	-3.8	-8.8	-9.6
178.7	MAT12-68	7544	-5.7	-5.7	-11.9	-12.8
179.9	MAT12-67	7547	-5.2	-5.2	-10.6	-11.5
182.0	MAT12-66	7553	-4.2	-4.3	-10.0	-11.0
184.4	MAT12-65	7559	-4.0	-4.1	-9.9	-10.9
186.5	MAT12-64	7564	-4.1	-4.1	-10.5	-11.6
188.5	MAT12-63	7570	-4.6	-4.7	-11.2	-12.3
190.0	MAT12-62	7574	-4.7	-4.7	-9.8	-11.0
191.7	MAT12-61	7578	-5.9	-5.9	-11.1	-12.4
193.0	MAT12-60	7582	-4.6	-4.6	-11.3	-12.6
195.2	MAT12-59	7587	-4.6	-4.6	-11.0	-12.3
197.8	MAT12-58	7594	-4.1	-4.2	-9.3	-10.7
199.9	MAT12-57	7600	-3.6	-3.7	-9.5	-11.0
202.0	MAT12-56	7605	-4.5	-4.6	-9.3	-10.9
204.8	MAT12-55	7613	-3.6	-3.6	-8.1	-9.8
206.9	MAT12-54	7618	-4.3	-4.4	-8.5	-10.2
209.0	MAT12-53	7624	-4.5	-4.5	-9.6	-11.2
210.8	MAT12-52	7628	-4.4	-4.5	-9.9	-11.5
212.8	MAT12-51	7634	-5.6	-5.7	-12.4	-13.9
214.7	MAT12-50	7639	-6.2	-6.3	-12.4	-13.9
217.5	MAT12-49	7646	-3.8	-3.9	-10.3	-11.7
220.2	MAT12-48	7653	-3.4	-3.4	-9.9	-11.1
222.0	MAT12-47	7658	-3.4	-3.5	-9.1	-10.3
224.0	MAT12-46	7663	-3.6	-3.7	-9.5	-10.6
226.2	MAT12-45	7669	-4.6	-4.7	-11.5	-12.6
228.9	MAT12-44	7676	-3.9	-3.9	-10.7	-11.6
231.0	MAT12-43	7682	-3.4	-3.5	-10.6	-11.5
233.2	MAT12-42	7687	-5.4	-5.4	-12.5	-13.2
235.1	MAT12-41	7692	-4.2	-4.2	-11.6	-12.4
236.7	MAT12-40	7715	-4.5	-4.6	-12.2	-13.1
238.3	MAT12-39	7720	-4.7	-4.8	-10.3	-11.3
240.0	MAT12-38	7725	-4.9	-4.9	-10.7	-11.7
242.4	MAT12-37	7732	-3.4	-3.4	-8.9	-10.0
244.2	MAT12-36	7737	-4.3	-4.3	-9.5	-10.6
246.0	MAT12-35	7743	-4.1	-4.2	-10.6	-11.8
249.0	MAT12-34	7752	-3.4	-3.5	-9.6	-10.9
250.8	MAT12-33	7757	-4.2	-4.3	-9.8	-11.2

Dft (mm)	Sample	Age (yr BP)	$\delta^{18}O$ (uncorrected)	$\delta^{18}O$ (corrected)	$\delta^{13}C$ (uncorrected)	$\delta^{13}C$ (corrected)
253.6	MAT12-32	7765	-4.6	-4.7	-10.7	-12.2
255.0	MAT12-31	7769	-3.9	-3.9	-8.8	-10.3
257.1	MAT12-30	7775	-4.2	-4.3	-9.4	-11.0
259.5	MAT12-29	7783	-4.8	-4.9	-9.1	-10.8
262.8	MAT12-28	7792	-5.2	-5.2	-12.0	-13.3
266.5	MAT12-27	7803	-5.4	-5.4	-11.2	-12.0
269.4	MAT12-26	7812	-5.4	-5.4	-11.8	-12.2
272.0	MAT12-25	7819	-4.9	-4.9	-12.7	-12.7
274.3	MAT12-24	7826	-4.8	-4.8	-12.5	-12.5
276.9	MAT12-23	7834	-5.8	-5.8	-12.4	-12.4
279.5	MAT12-22	7841	-5.4	-5.4	-12.0	-12.0
283.4	MAT12-21	7910	-4.1	-4.1	-10.1	-10.1
285.8	MAT12-20	7916	-4.4	-4.4	-11.1	-11.1
289.0	MAT12-19	7924	-4.8	-4.8	-12.3	-12.3
292.3	MAT12-18	7931	-4.3	-4.3	-11.8	-11.8
295.0	MAT12-17	7938	-5.6	-5.6	-11.9	-11.9
297.0	MAT12-16	7943	-6.8	-6.8	-12.4	-12.4
299.9	MAT12-15	7950	-5.7	-5.7	-12.5	-12.5
302.9	MAT12-14	7957	-5.7	-5.7	-12.4	-12.6
305.1	MAT12-13	7962	-5.0	-5.0	-12.4	-12.7
308.4	MAT12-12	7970	-5.5	-5.5	-12.1	-12.8
310.4	MAT12-11	7975	-4.9	-5.0	-11.3	-12.1
312.7	MAT12-10	7981	-4.9	-4.9	-11.7	-12.7
314.9	MAT12-9	7986	-5.4	-5.4	-11.4	-12.6
317.2	MAT12-8	7991	-4.0	-4.0	-10.3	-11.6
319.5	MAT12-7	7997	-5.8	-5.9	-11.4	-13.0
322.5	MAT12-6	8004	-5.5	-5.6	-11.6	-13.3
325.8	MAT12-5	8012	-5.6	-5.7	-12.0	-13.7
327.7	MAT12-4	8017	-5.8	-5.9	-10.9	-12.6
330.0	MAT12-3	8022	-4.6	-4.6	-9.6	-11.3
332.4	MAT12-2	8028	-4.6	-4.6	-10.5	-12.2
334.8	MAT12-1	8034	-5.0	-5.1	-11.6	-13.3